iScience

Article

Mutation T9I in Envelope confers autophagy resistance to SARS-CoV-2 Omicron

Graphical abstract

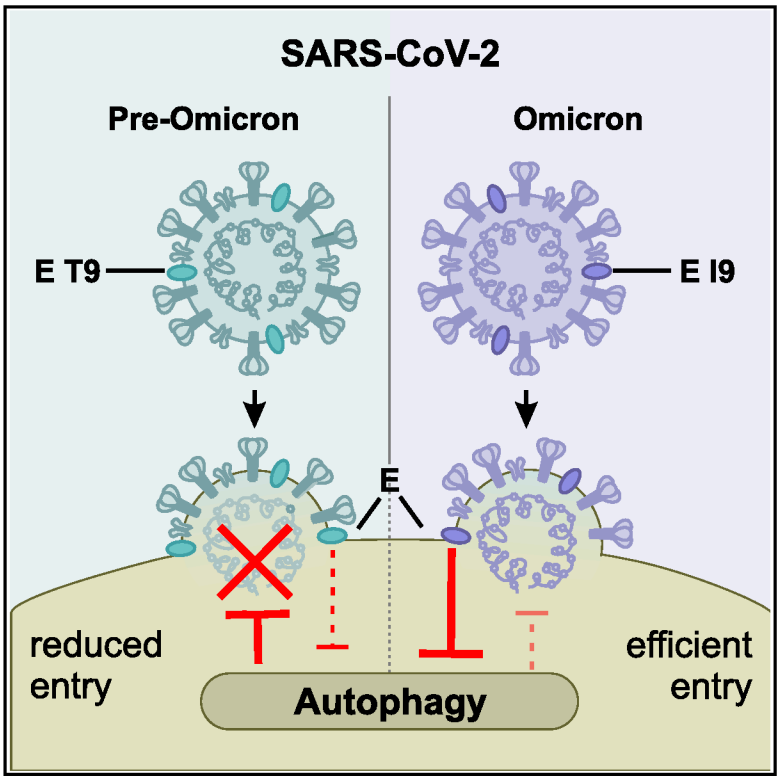

Authors

Susanne Klute, Rayhane Nchioua, Arne Cordsmeier, ..., Andreas Pichlmair, Armin Ensser, Konstantin Maria Johannes Sparrer

Correspondence

konstantin.sparrer@uni-ulm.de

In brief

Natural sciences; Biological sciences; Microbiology; Cell biology

Highlights

- Omicron-associated E T9I renders incoming SARS-CoV-2 resistant to autophagy
- T9I promotes interaction of E with autophagy-associated factors and autophagosomes
- Autophagy evasion may have contributed to the effective spread of Omicron

Klute et al., 2025, iScience 28, 112974
July 18, 2025
https://doi.org/10.1016/j.isci.2025.112974

CellPress

iScience

CellPress
OPEN ACCESS

Article

Mutation T9I in Envelope confers autophagy resistance to SARS-CoV-2 Omicron

Susanne Klute,[1] Rayhane Nchioua,[1] Arne Cordsmeier,[2] Jyoti Vishwakarma,[3] Lennart Koepke,[1] Hala Alshammary,[1,4,5] Christoph Jung,[6,7,8] Maximilian Hirschenberger,[1] Helene Hoenigsperger,[1] Jana-Romana Fischer,[1,9] Rinu Sivarajan,[1] Fabian Zech,[1] Steffen Stenger,[10] Ruth Serra-Moreno,[11] Ana Silvia Gonzalez-Reiche,[12] Emilia Mia Sordillo,[13] Harm van Bakel,[4,12,14] Viviana Simon,[4,5,13,15,16] Frank Kirchhoff,[1] Timo Jacob,[6] Dorota Kmiec,[1] Andreas Pichlmair,[3] Armin Ensser,[2] and Konstantin Maria Johannes Sparrer[1,9,17,*]

[1]Institute of Molecular Virology, Ulm University Medical Center, 89081 Ulm, Baden-Württemberg, Germany
[2]Institute for Clinical and Molecular Virology, University Hospital, Friedrich-Alexander-Universität Erlangen-Nürnberg, 91054 Erlangen, Bavaria, Germany
[3]Institute of Virology, School of Medicine, Technical University of Munich, 80333 Munich, Bavaria, Germany
[4]Department of Microbiology, Icahn School of Medicine at Mount Sinai, New York, NY 10029, USA
[5]Center for Vaccine Research and Pandemic Preparedness (C-VaRPP), Icahn School of Medicine at Mount Sinai, New York, NY 10029, USA
[6]Institute of Electrochemistry, Ulm University, 89081 Ulm, Baden-Württemberg, Germany
[7]Helmholtz-Institute Ulm (HIU) Electrochemical Energy Storage, 89081 Ulm, Baden-Württemberg, Germany
[8]Karlsruhe Institute of Technology (KIT), 76131 Karlsruhe, Baden-Württemberg, Germany
[9]German Center for Neurodegenerative Diseases (DZNE), 89081 Ulm, Baden-Württemberg, Germany
[10]Institute of Medical Microbiology and Hygiene, Ulm University Medical Center, 89081 Ulm, Baden-Württemberg, Germany
[11]Department of Microbiology and Immunology, University of Rochester, Rochester, NY 14642, USA
[12]Department of Genetics and Genomic Sciences, Icahn School of Medicine at Mount Sinai, New York, NY 10029, USA
[13]Department of Pathology, Molecular, and Cell-Based Medicine, Icahn School of Medicine at Mount Sinai, New York, NY 10029, USA
[14]Icahn Genomics Institute, Icahn School of Medicine at Mount Sinai, New York, NY 10029, USA
[15]Division of Infectious Diseases, Department of Medicine, Icahn School of Medicine at Mount Sinai, New York, NY 10029, USA
[16]The Global Health and Emerging Pathogens Institute, Icahn School of Medicine at Mount Sinai, New York, NY 10029, USA
[17]Lead contact
*Correspondence: konstantin.sparrer@uni-ulm.de
https://doi.org/10.1016/j.isci.2025.112974

SUMMARY

Omicron has emerged as the most successful variant of SARS-CoV-2. In addition to mutations in Spike that mediate humoral immune escape, the Omicron-specific Envelope (E) T9I mutation has been associated with increased transmission fitness. However, the underlying mechanism remained unclear. Here, we demonstrate that the E T9I mutation confers resistance to autophagy. Rare Omicron patient isolates encoding the ancestral E T9 remain sensitive to autophagy. Conversely, introducing the E T9I mutation in recombinant 2020 SARS-CoV-2 renders it resistant to autophagy. Our data indicate that the E T9I mutation protects virions against lysosomal degradation. At the molecular level, the T9I mutation increases the localization of E at autophagic vesicles and promotes interaction with autophagy-associated proteins SNX12, STX12, TMEM87B, and ABCG2. Our results show that the E T9I mutation renders incoming virions resistant to autophagy, suggesting that evasion of this antiviral mechanism contributes to the efficient spread of Omicron.

INTRODUCTION

The severe acute respiratory syndrome coronavirus 2 (SARS-CoV-2) is the causative agent of the COVID-19 pandemic.[1,2] After crossing the species barrier from bats to humans, most likely through an as-yet unidentified intermediate host at the end of 2019 [1], SARS-CoV-2 has been adapting to its human host.[3] Altogether, five variants of SARS-CoV-2 (Alpha, Beta, Gamma, Delta, and Omicron) with increased transmission and immune evasion capacity, termed variants of concern (VOC), emerged over the past five years.[3] Omicron rapidly outcompeted all previous variants and currently (April 2025), various subvariants including XEC and LP.8.1 are prevalent.[4–10] Omicron acquired distinct mutations that increase transmission fitness.[11] Most changes cluster in the gene encoding the viral Spike (S) protein[11] and allow Omicron to evade humoral immune responses induced by previous vaccination or SARS-CoV-2 infection.[12–14] However, an analysis of 6.4 million SARS-CoV-2 genomes identified four non-Spike mutations that are associated with increased viral transmission fitness: ORF1a P3395H, ORF1a K856R, E T9I and ORF9b P10S.[15] The underlying mechanisms remained unclear.

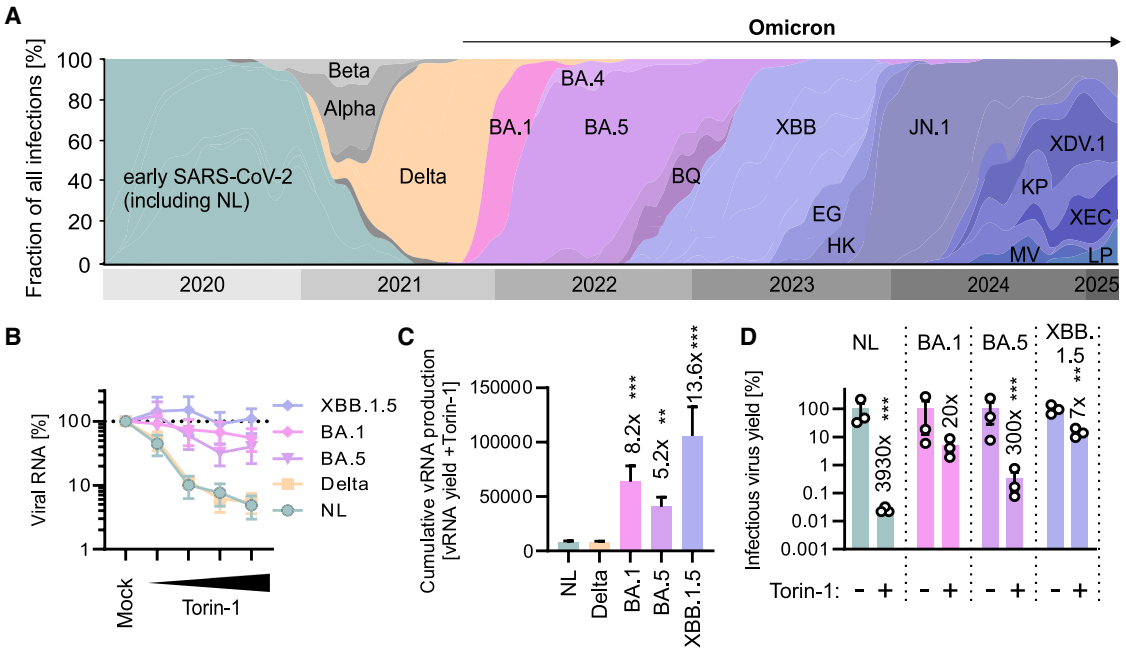

Figure 1. The Omicron VOC is less sensitive against autophagy

(A) Relative abundance of indicated SARS-CoV-2 strains until March 2025, Data from Nextstrain, retrieved March 2025 (B) Quantification of SARS-CoV-2 N viral RNA in the supernatant of Calu-3 cells infected with indicated SARS-CoV-2 strains (MOI 0.05) and treated with increasing amounts of Torin-1 (0.016–1 μM) by qRT-PCR 48 h post infection. Dots represent the mean of N = 3–6 (biological replicates) ±SEM.

(C) Area under the curve analysis of the data in (B). Bars represent the mean of N = 3–6 (biological replicates) +SEM.

(D) Infectious SARS-CoV-2 in the supernatant of Calu-3 cells treated with 250 nM Torin-1 or left untreated and infected with indicated viruses (MOI 0.05) as assessed by TCID50. Bars represent the mean of *N* = 3 (biological replicates) ±SEM. Student's *t* test with Welch's correction. **, $p < 0.01$; ***, $p < 0.001$.

In addition to adaptive immunity, innate immune mechanisms, such as autophagy, are important in the defense against SARS-CoV-2.[16–20] Autophagy is an evolutionarily conserved catabolic pathway and innate defense mechanism that targets viral particles or components for lysosomal degradation.[21–24] The cargo is recognized by autophagy receptors, such as Sequestome-1 (p62/SQSTM1) and engulfed in Microtubule-associated protein 1 light chain 3 beta II (LC3B-II)-positive double-membrane vesicles called autophagosomes.[25,26] Subsequently, autophagosomes fuse with lysosomes and the cargo, along with the receptor, is degraded. To avoid lysosomal degradation, SARS-CoV-2 perturbs autophagy. Infection with SARS-CoV-2 leads to accumulation of p62/SQSTM1 and LC3B-II *in vitro* and *in vivo*, indicating impaired autophagic turnover.[17,18] While many different SARS-CoV-2 proteins manipulate autophagy,[18,27] the E protein is the only structural viral protein that inhibits autophagic flux.[18] The 75 amino acid long E protein assembles into a viroporin consisting of five membrane-spanning E proteins and enabling ion channel activity.[28,29] Intracellularly, E localizes to endosomes and lysosomes, triggers endoplasmic reticulum stress responses and affects host cell survival.[30,31] However, the precise role of E in incoming virions is poorly understood. Here, we show that the T9I mutation in E, which emerged with the Omicron lineage, confers resistance to autophagy and protects incoming virions. Thus, our results indicate that escape from autophagy contributed to the dominance of the Omicron variant.

RESULTS

The Omicron variant of SARS-CoV-2 is resistant to autophagy

The emergence of Omicron marked a significant shift in SARS-CoV-2 evolution, and the new variant and its subvariants (e.g., BA.1, BA.2, and XBB) rapidly outcompeted earlier SARS-CoV-2 strains due to their superior immune evasion (Figure 1A). We examined whether SARS-CoV-2 Omicron adapted to escape not only adaptive but also innate immune defenses, such as autophagy. Therefore, we analyzed the impact of autophagy activation by Torin-1[32] on the replication of various SARS-CoV-2 VOCs in Calu-3 cells. Our data show that Torin-1 treatment inhibited replication of an early 2020 SARS-CoV-2 isolate (NL-02-2020, hereafter NL), as well as the Delta variant, in a dose-dependent manner by up to 25-fold (Figures 1B and S1A). In contrast, all tested Omicron variants were largely (BA.1 and BA.5) or fully (XBB.1.5) resistant to autophagy (Figure 1B). Cumulative viral RNA production by BA.1, BA.5, or XBB.1.5 was 8.2-, 5.2- and 13.6-fold less affected by Torin-1 compared to NL (Figure 1C). It was previously suggested that mTOR targeting promotes SARS-CoV-2 infection by inducing the expression of interferon (IFN) induced transmembrane proteins (IFITMs).[33] However, endogenous IFITM levels were unaffected by Torin-1 in Calu-3 cells despite robust autophagy induction as indicated by decreased endogenous

p62/SQSTM1 levels (Figures S1B–S1E). Autophagy resistance of Omicron variants was confirmed by determining viral titers 48 h post-infection (Figures 1D and S1F). Treatment with 250 nM Torin-1 reduced infectious viral yields of NL by almost 4000-fold, but had only 20-, 300- and 7-fold effects on Omicron subvariants BA.1, BA.5, and XBB.1.5. (Figure 1D). Torin-1 activates autophagy by inhibition of Mechanistic target of rapamycin (mTOR). Thus, Omicron variants have evolved reduced sensitivity to autophagy compared to ancestral SARS-CoV-2 strains and previous VOCs.

The Omicron-specific T9I mutation in E leads to increased autophagosome accumulation

To unravel the mechanism underlying autophagy evasion by Omicron, we focused on three viral proteins previously shown to antagonize autophagic flux[17,18]: ORF3a, ORF7a and E. The Delta and the Omicron VOCs harbor distinct consensus mutations in these three genes compared to NL/Hu-1: Delta (ORF3a S26L, ORF7a V82A, T120I), BA.1 (E T9I), BA.5 (ORF3a T223I; E T9I), XBB.1.5 (ORF3a T223I; E T9I, and T11A) (Figure 2A). We introduced single point mutations in NL-derived ORF3a, ORF7a, and E by site-directed mutagenesis (Figure 2B). To analyze the impact of the mutations on autophagy, we employed a flow cytometry-based system.[34,35] In brief, HEK293T cells stably expressing the autophagy marker protein green fluorescent protein (GFP)-LC3B are mildly permeabilized by saponin. Membrane-bound GFP-LC3B, which decorates autophagosomes, remains associated to the cells. Thus, the remaining GFP fluorescence serves as a proxy for autophagosome content of a cell. Expression of VOC-associated SARS-CoV-2 constructs revealed that ORF3a S26L, ORF7a V82A, and ORF7a T120I caused similar levels of autophagosome accumulation as the corresponding parental proteins. Mutation of T223I in ORF3a slightly increased autophagosome levels compared to wild-type (WT) ORF3a, albeit non-significantly. However, expression of the Omicron-derived E T9I variant resulted in a robust and significantly greater autophagosome accumulation compared to its NL-derived counterpart (E WT) (Figure 2B). Dose-dependency assays revealed that E T9I outperforms E T9 over a broad range of expression levels (Figure 2C). To discern whether E increases autophagosome levels due to increased autophagic flux or impaired autophagosome turnover, we monitored endogenous LC3B-I to LC3B-II conversion, as well as p62/SQSTM1 levels, two hallmarks of autophagic flux.[35] In the presence of E LC3B-II and p62 accumulate, suggesting that it inhibits autophagic flux (Figure 2D). To corroborate that E inhibits autophagosome turnover, we stopped autophagosome-lysosome fusion using saturating concentrations of Bafilomycin A1.[35] Expression of both E variants did not increase cellular autophagosome levels in the presence of Bafilomycin A1 significantly[35] (Figure 2E). Finally, accumulation of autophagosomes in the presence of E T9I compared to E T9 was confirmed by quantifying GFP-LC3B-positive puncta (=autophagosomes) in HeLa autophagy reporter cells transiently expressing wild-type E T9 or E T9I (Figure 2F). In summary, these results indicate that the T9I mutation enhances the ability of SARS-CoV-2 E to antagonize autophagic flux.

Rare naturally occurring Omicron variants with E T9 are autophagy sensitive

Coinciding with the emergence of the Omicron VOC in late November 2021, E T9I rapidly became predominant in the circulating SARS-CoV-2 strains (Figures 3A and 3B). In previous variants, E T9I was only sporadically (<1%) present (Figure 3A, data from Nextstrain, January 2025). In 2023, 97.28% of all sequences available of circulating SARS-CoV-2 encoded the E I9 substitution, while only 0.76% retained the T at position 9, with 1.95% contained an undefined amino acid at position 9 (Figure 3C, data from CovSpectrum, January 2024[36]). Utilizing the ongoing surveillance of circulating SARS-CoV-2[37–39] at the Mount Sinai Health System (MSHS), we identified rare SARS-CoV-2 Omicron variants retaining E T9 (Figures 3D and S2A). To explore the phenotype of these authentic SARS-CoV-2 strains, we isolated and cultured two closely related isolates Omicron BA.2 with E T9 (USA/NY-MSHSPSP-PV58179/2022, EPI_ISL_12711111) (Figures 3D and S2A) and with E T9I (USA/NY-MSHSPSP-PV58079/2022, EPI_ISL_12711042) (Figures 3D and S2A). On Calu-3 cells PV58179 (E T9) grew to approximately 10-fold higher titers than the PV58079 (E T9I) isolate (Figure 3E). Treatment with Torin-1 during the infection reduced replication of E T9 PV58179 more than 4-fold but did not impact E T9I PV58079 (Figure 3E). These data suggest that the T9I mutation in E may limit SARS-CoV-2 replication speed but confers resistance to autophagy.

T9I in E increases resistance of recombinant SARS-CoV-2 to autophagy

To clarify whether mutation of E T9I is sufficient to confer resistance against autophagy, we generated recombinant SARS-CoV-2 (rSARS-CoV-2) harboring E T9I in an ancestral 2020 SARS-CoV-2 background (rSARS2-E-T9 and rSARS2-E-T9I) (Figure S2B).[40] Growth analyses revealed that rSARS2-E-T9I replicated to ~10- to 50-fold lower titers than rSARS2-E-T9 (Figure 3F). However, rSARS2-E-T9 was highly sensitive to autophagy induction by Torin-1 (Figure 3G). In comparison, rSARS2-E-T9I replicated less efficiently but was largely resistant to autophagy induction (Figure 3G). In autophagy-defective MRC5-ACE2 cells (*ATG5* KO MRC5-ACE2), rSARS2-E-T9 grew significantly faster than in WT MRC5-ACE2 cells (Figure 3H), suggesting that autophagy reduces its replication. In comparison, WT and T9I mutant SARS-CoV-2 replicated with similar kinetics in *ATG5* KO MRC5-ACE2 (Figure 3H). In summary, the E T9I mutation confers resistance to autophagy to recombinant SARS-CoV-2 at the cost of reduced replication capacity.

Impact of T9I mutation on E pore and intracellular localization

The E protein of SARS-CoV-2 assembles as a pentameric alpha-helical complex in lipid bilayers, forming an ion channel permissive for Ca^{2+}, K^{+}, Na^{+} ions in a pH-dependent manner.[41] It consists of an N-terminal domain (NTD), a hydrophobic transmembrane domain (TMD) and a C-terminal domain (CTD) (Figure 4A). While T9 is located at the TMD of E, it is not directly part of the pore-forming core transmembrane helix.[29] To examine the impact of T9I on pore size, we performed molecular dynamics modeling leveraging a previously published NMR

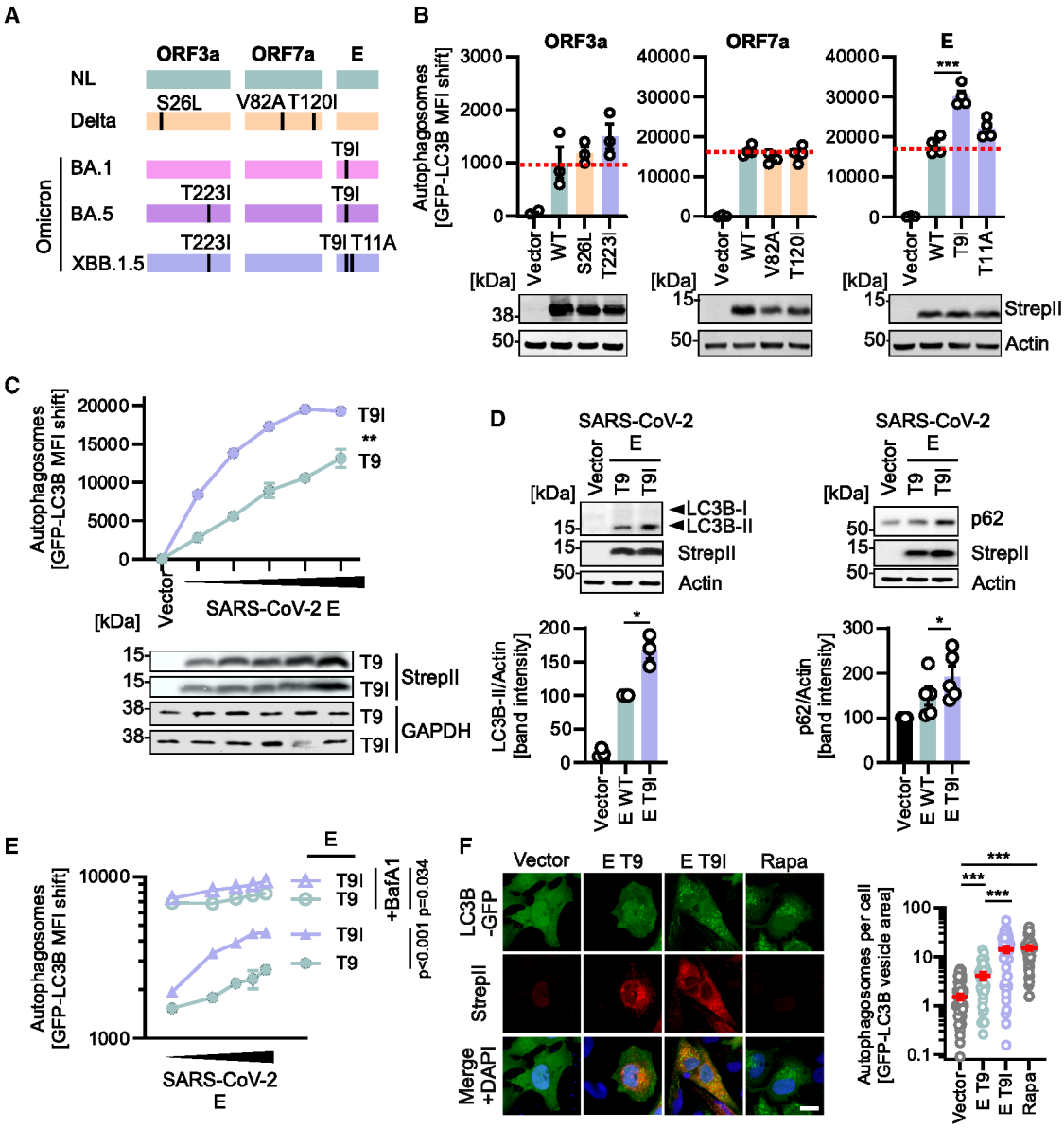

Figure 2. Mutation T9I enhances autophagy antagonism of E

(A) Schematic depiction of the major autophagy antagonists of SARS-CoV-2, ORF3a, ORF7a and E (Envelope). Specific VOC-associated mutations compared to early 2020 SARS-CoV-2 (NL) are annotated.

(B) Quantification of autophagosome levels by flow cytometry in HEK293T autophagy reporter cells (HEK293T-GL) transiently expressing StrepII-tagged SARS-CoV-2 proteins (48 h post transfection). Bars represent the mean of $N = 3$-4 (biological replicates) ±SEM. (Top panels). Immunoblots stained with anti-StrepII and anti-Actin. (Bottom panels).

(C) Quantification of autophagosome levels by flow cytometry in HEK293T autophagy reporter cells (HEK293T-GL) transiently expressing increasing amounts of StrepII-tagged SARS-CoV-2 E T9 or E T9I (48 h post transfection). Bars represent the mean of $N = 3$ (biological replicates) ±SEM. (Top panel). Representative immunoblots stained with anti-StrepII and anti-GAPDH. (Bottom panel).

(D) Representative immunoblots of HEK293T-GL cells overexpressing SARS-CoV-2 E proteins (B) were stained with anti-p62, anti-LC3B, anti-StrepII and anti-Actin. Quantification of LC3B-II/Actin and p62/Actin band intensities, as indicated, of three independent immunoblots detecting SARS-CoV-2 E proteins. Bars represent the mean of $N = 3$-5 (independent experiments) ±SEM.

(E) Quantification of autophagosome levels by flow cytometry in HEK293T-GL cells transiently expressing increasing amounts of StrepII-tagged SARS-CoV-2 E T9 and E T9I (48 h post transfection) and treated with 250 nM Bafilomycin A1 (empty symbols) or medium (filled symbols) 4 h before harvest. Dots represent the mean of $N = 4$ (biological replicates) ±SEM. One-way ANOVA, p values indicated.

(F) Representative confocal immunofluorescence images of HeLa-GFP-LC3B (green) cells transiently expressing StrepII tagged SARS-CoV-2 E T9 and E T9I (red) or treated with Rapamycin (Rapa; 1 μM, 24 h) (scale bar, 10 μm). DAPI, nuclei (blue). (Left panel). Quantification of the number of autophagosomes (=GFP-LC3B positive puncta) in the images in the left panel. Lines represent the mean of $N = 35$–110 (individual cells) ±SEM. (Right panel). Student's t test with Welch's correction. *, $p < 0.05$; **, $p < 0.01$; ***, $p < 0.001$.

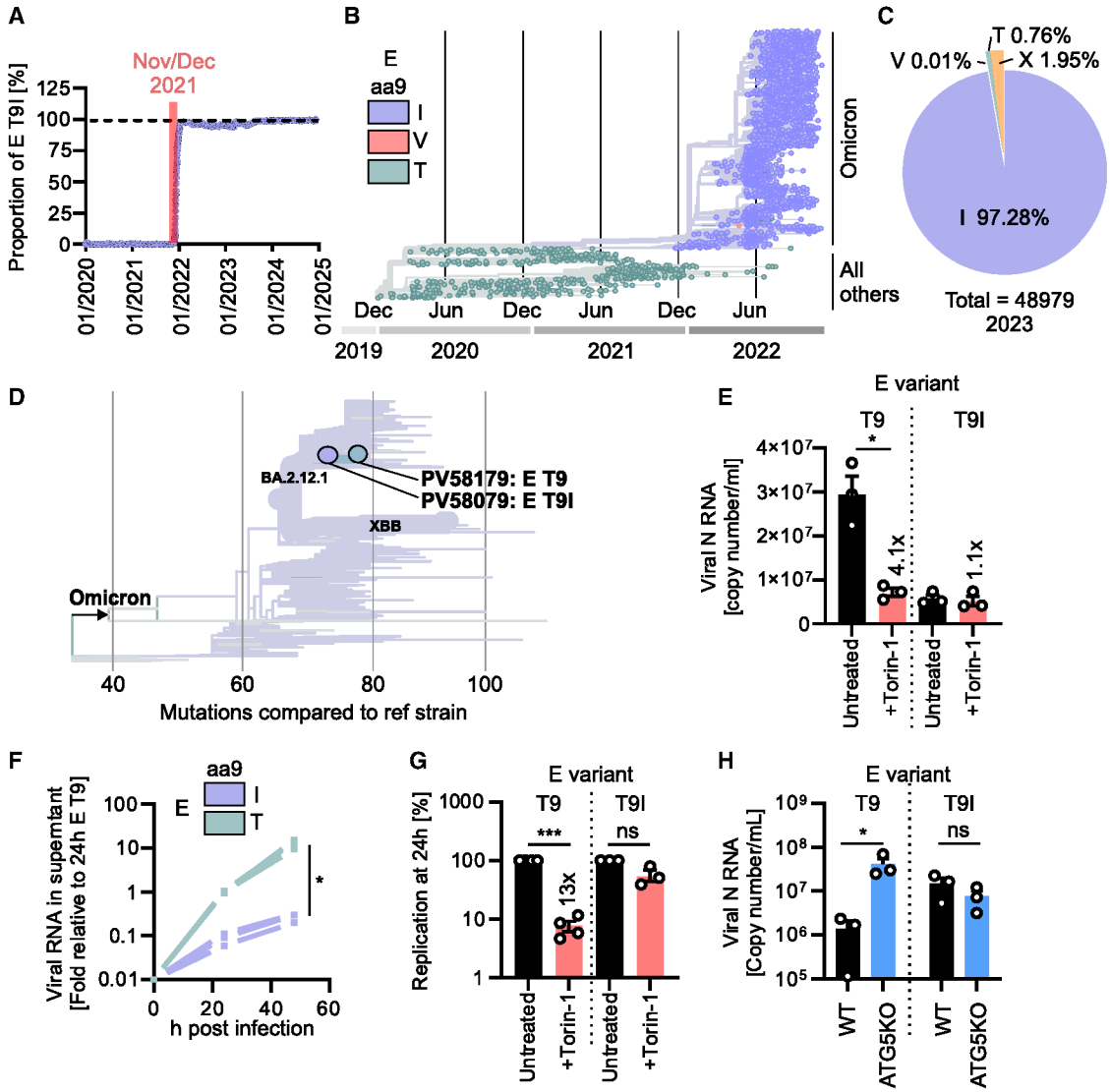

Figure 3. T9I E promotes autophagy resistance of patient-isolated and recombinant SARS-CoV-2

(A) Ratio of E T9I mutation in all SARS-CoV-2 strains sampled from 01/2020 to 01/2025. Nov/Dec 2021 is highlighted in red. Data sourced from covspectrum.org, January 2025.

(B) Phylogenetic tree of SARS-CoV-2 variants since early 2020, sourced from Nextstrain, November 2023. Amino acid at position 9 in E is highlighted by colors.

(C) Percentages of amino acid residues at position 9 in E of 48979 Omicron strains.

(D) Excerpt of a phylogenetic tree showing the collection of SARS-CoV-2 isolates from the Mount Sinai surveillance program. The relation between E T9 coding PV58179 and E T9I coding PV58079 isolates is highlighted.

(E) Absolute quantification of viral RNA in the supernatant of Calu-3 cells mock treated or treated with Torin-1 (250 nM) and infected with SARS-CoV-2 patient isolates PV58079 or PV58179 (MOI 0.05) as assessed by qRT-PCR 48 h post infection. Bars represent the mean of $N = 3$ (biological replicates) ±SEM.

(F) Relative quantification of viral RNA in the supernatant of Calu-3 cells infected with rSARS2-E T9 or rSARS2-E T9I as assessed by qRT-PCR 24 h and 48 h post infection. 24 h rSARS2-E T9 is set to 1. Dots represent the mean of $N = 4$ (biological replicates) ±SEM.

(G) Relative quantification of viral RNA in the supernatant of Calu-3 cells treated or non-treated with Torin-1 (250 nM) and infected with rSARS2-E T9 or rSARS2-E T9I (MOI 0.05) as assessed by qRT-PCR 24 h post infection. 24 h mock treated values are set to 100%. Bars represent the mean of N = 3–4 (biological replicates) ±SEM.

(H) Quantification of viral RNA in MRC5-ACE2 WT or *ATG5* KO cells by qRT-PCR at 72 h post infection with SARS2-E T9 or rSARS2-E T9I (MOI 0.05). Bars represent the mean of $N = 3$ (biological replicates) ±SEM. Student's *t* test with Welch's correction. *, $p < 0.05$; ***, $p < 0.001$. ns (non-significant).

structure of E (PDB: 7K3G).[29] This analysis suggested that the T9I mutation has a minimal impact on pore size, with the WT E T9 and mutant E T9I exhibiting pore sizes of 14.17 Å and 13.61 Å, respectively (Figures 4B–4D). To assess whether the viroporin function of E affects autophagy, we employed an E viroporin inhibitor (BIT225).[42] Treatment with non-cytotoxic concentrations of BIT225 had no impact on autophagosome accumulation mediated by E in HEK293T autophagy reporter

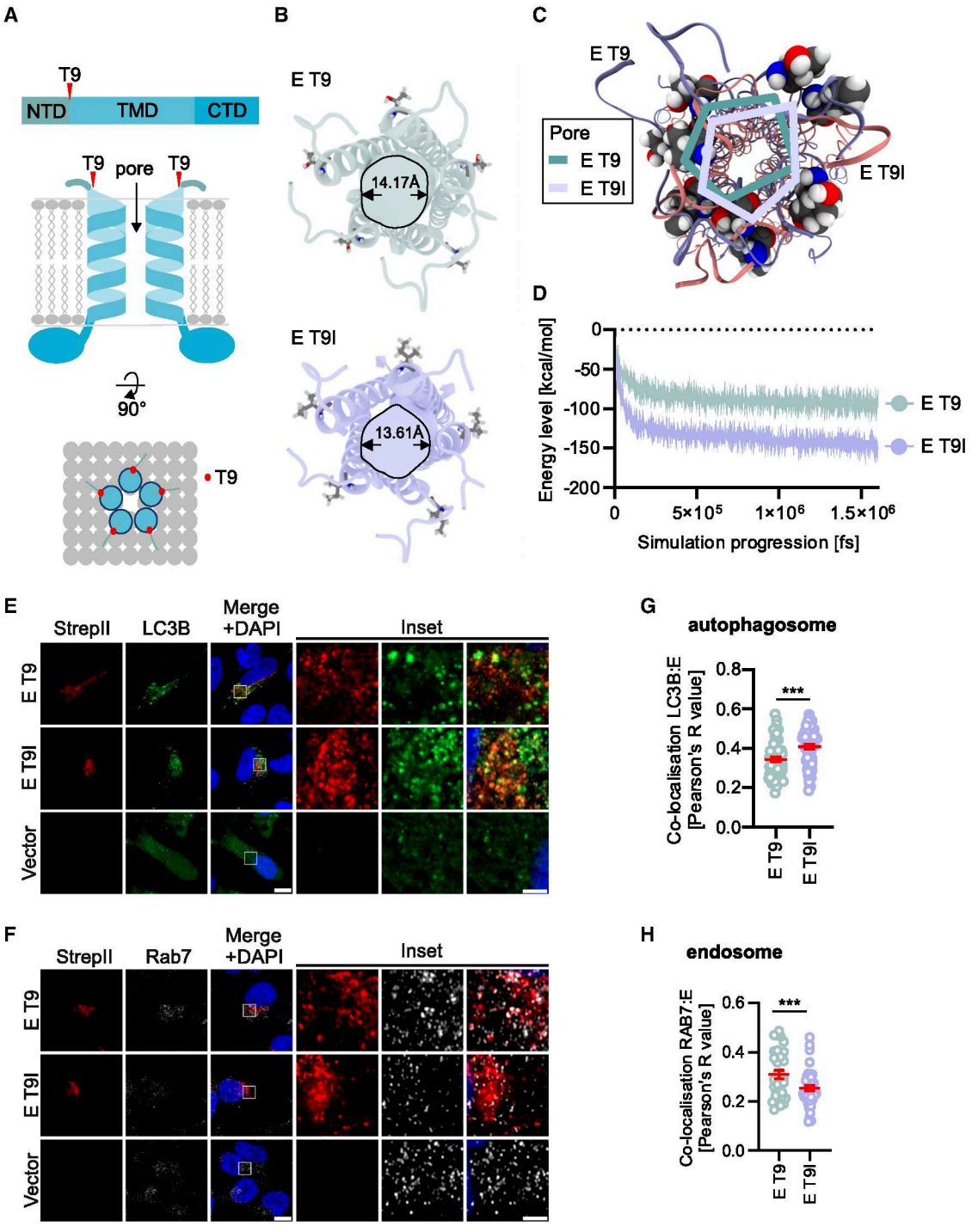

Figure 4. Impact of mutation T9I on E viroporin assembly and intracellular localization

(A) Schematic depiction of the structure of SARS-CoV-2 E. NTD, N-terminal domain. TMD, Transmembrane domain. CTD, C-terminal domain. The position of T9 in E is highlighted in red.

(B) Schematic representation of the E protein ion channel depicted as a cartoon showing a transmembrane view. The ninth amino acid is highlighted as a stick, with the colors representing carbon (gray), oxygen (red) and hydrogen (white). The diameter of E protein ion channels is depicted in Ångström (Å).

(C) Visualization of the lateral projection surface of the E ion channel pore. Each case is an example image from the trajectory of the molecular dynamics simulation.

(D) Representative energy curve of the reactive molecular dynamics simulation for SARS-CoV-2 E T9 and E T9I.

(legend continued on next page)

cells (Figures S3A and S3B). Previous data showed that E mainly localizes to intracellular vesicles such as lysosomes, late endosomes, and autophagosomes.[18,31] High resolution point-scan microscopy of HeLa-GFP-LC3B cells transiently expressing either E T9 or E T9I, suggested that both variants localize to LC3B-positive autophagosomes and Ras-related protein 7a (Rab7a)-positive late endosomes albeit to varying degrees (Figures 4E and 4F). E T9I was less present at late endosomes but showed increased localization to autophagosomes (Figures 4E and 4F). To quantify this, we performed confocal microscopy of over 70 randomly selected cells and calculated the colocalization between E and LC3B or E and Rab7a (Pearson correlation coefficient). This showed that E T9I shifts from Rab7a-positive vesicles to LC3B-positive autophagosomes (Figures 4G, 4H, S3C, and S3D). Taken together, these data suggest that the T9I mutation in E does not affect its viroporin function but increases the localization of E to autophagosomes.

E T9I increases autophagy resistance of virions

Autophagy targets incoming virions for lysosomal degradation.[22,43] Thus, only structural proteins may promote autophagy evasion upon entry. To define the impact of E on virion entry and separate it from replication, we used Vesicular Stomatitis Virus-based pseudoparticles (VSVpp), which recapitulate major steps of SARS-CoV-2 entry.[14,44,45] To this end, we pseudotyped VSV that expressed GFP instead of its Glycoprotein (G) with SARS-CoV-2 S (VSVpp*S) and either E T9 or E T9I (Figure S4A). The presence of SARS-CoV-2 E and S in the VSVpp*S was verified by immunoblotting (Figure 5A). E T9 and E T9I were incorporated with similar efficiency into VSVpp*S (Figure S4C). The presence or absence of E had no significant effect on SARS-CoV-2 S and VSV M particle production in the presence or absence of autophagy (*ATG5* KO cells) (Figures 5A, S4B, and S4D). S incorporation levels into VSVpp were confirmed by ELISA (Figure 5B). Previous studies suggested that E may affect the functionality and processing of virion-associated S.[28] However, immunoblotting analyses showed that S in the supernatant was processed similarly in the presence of E T9 or E T9I (Figure 5A). An Angiotensin-converting enzyme 2 (ACE2)-S interaction assay revealed that E T9 and E T9I do not impact the receptor binding capacity of the VSVpp*S (Figure 5C). To assess the impact of autophagy on incoming virions, we treated Caco-2 cells with Torin-1 before infection. Autophagy induction reduced infection with single-round VSVpp*S by about 50% (Figures 5D and S4E). The presence of E T9 in the particles only marginally altered autophagy resistance of the VSVpp*S. In contrast, VSVpp*S carrying E T9I were almost completely resistant toward Torin-1 treatment (Figure 5D). Infection of WT MRC5-ACE2 by VSVpp*S carrying E T9I was more efficient than infection with VSVpp*S carrying E T9. However, the advantage of having E T9I in the virion was lost in autophagy-negative MRC5-ACE2 cells (ATG5 KO) (Figure 5E). Collectively, these results suggest that the presence of E T9I in VSV particles pseudotyped with SARS-CoV-2 S does not affect particle assembly or intrinsic infectivity but conveys resistance to autophagy.

E T9I increases interaction with autophagy-associated proteins

To further clarify whether the T9I mutation in E impacts its interaction with the autophagic machinery, we performed a differential interactome analysis. E T9 or E T9I were purified from stably E expressing A549 cells along with their cellular interaction partners which were identified by mass spectrometry (Data S1). Principal component analysis revealed that the E T9 and E T9I interactomes cluster differentially, indicating altered primary interaction partners (Figure 6A). Next, we used Gene ontology (GO) analysis to determine the biological processes associated with the proteins interacting with E T9I. Our results indicate that proteins binding more strongly to E T9I (fold change >2 and $p < 0.005$) are associated with biological processes like Endosomal Transport (GO:0016197), Endocytic Recycling (GO:0032456), Vesicle-Mediated Transport To The Plasma Membrane (GO:0098876), and Retrograde Transport or Endosome To Golgi (GO:0042147) (Figure S5A, Data S2). Volcano plot analyses of the aggregated replicates showed that STX12, SNX12, TMEM87B, ABCG2 and TAB1 were among the most significantly enriched proteins in the E T9I fraction (Figures 6B and S5B). STX12 (Syntaxin-12) regulates late endosomes and the trans-Golgi protein transport and was also reported to be required for autophagosome formation.[46] SNX12 (Sorting nexin 12) regulates cargo sorting in endosomes and plays a key role in autophagosome assembly.[47] TMEM87B (Transmembrane protein 87B) was predicted to be involved in endosome to Golgi transport.[48] ABCG2 (ATP-binding cassette superfamily G member 2) was shown to enhance autophagy.[49] Members of the protein family of TAB (Transforming growth factor β activated kinase 1 binding protein), such as TAB2 and TAB3, but not TAB1, were reported to inhibit autophagy.[50] To determine whether the mutation T9I alters the spatial proximity of E with the five candidate interaction partners, we performed proximity ligation assays (PLA) in HeLa cells (Figures 6C–6G and S5C). These data revealed that E T9I increased recruitment to SNX12, STX12, TMEM87B, and ABCG2, whereas the proximity to TAB1 was not affected. Interaction was confirmed by co-immunoprecipitation of endogenous TMEM87B, ABCG2 and STX12, which all readily co-purified SARS-CoV-2 E T9I in HEK293T cells (Figure S6). To understand whether these interactions are required for the autophagy function of E, we depleted HEK293T autophagy reporter cells of STX12, SNX12, TMEM87B, ABCG2, or TAB1 using siRNAs. qPCR analyses revealed a knockdown efficiency of >90% (Figure S5D). Analysis of the autophagosome levels upon overexpression of E using flow cytometry showed that depletion of SNX12, STX12, TMEM87B and ABCG2, but not TAB1, nearly fully abrogated

(E and F) Representative confocal scanning microscopy images of HeLa-GL cells transiently expressing StrepII-tagged SARS-CoV-2 E (red), co-stained anti-LC3B (green) (E) and anti-Rab7 (white) (F). Scale Bar full size images, 10 μm. Scale bar insets, 2 μm. DAPI, nuclei (blue).

(G and H) Quantification of the co-localization between E variants and the co-stained marker LC3B (S3C) and Rab7 (S3D) in confocal scanning microscopy images using Pearson's correlation. Lines represented the mean of $N = 33–73$ (individual cells) ±SEM. Student's *t* test with Welch's correction. ***, $p < 0.001$. ns (non-significant).

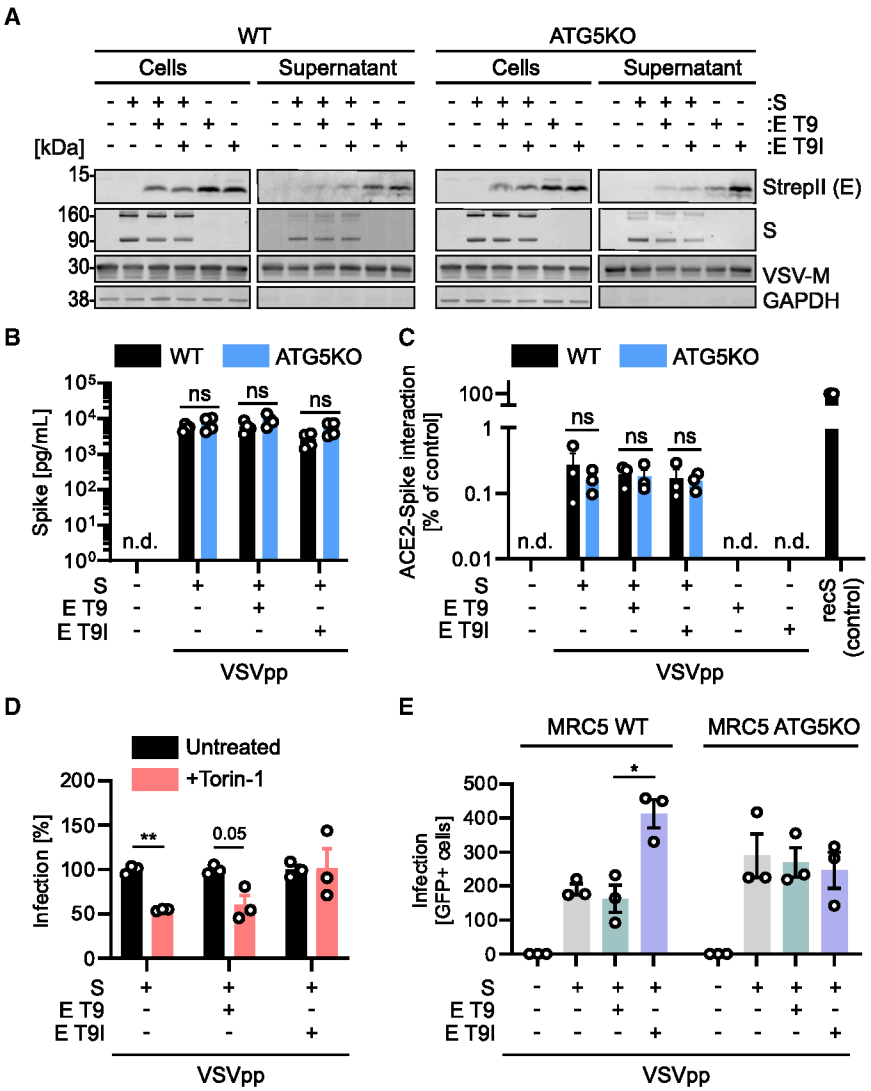

Figure 5. VSV pseudoparticles carrying E T9I are less sensitive toward autophagy

(A) Representative immunoblots of whole cell lysates and supernatants of HEK293T WT (left panel) and *ATG5* KO HEK293T (right panel) cells transiently expressing SARS-CoV-2 S (Hu-1), E T9 or E T9I as indicated and infected with VSV-ΔG-GFP*VSV-G (MOI 3). Blots were stained with anti-StrepII (E), anti-V5 (Spike), anti-VSV-M and anti-GAPDH.

(B) Concentration of S in VSVpp containing supernatants of HEK293T WT and *ATG5* KO cells in (A) assessed by Spike-ELISA. Bars represent the mean of $N = 4$ (independent experiments) ±SEM.

(C) ACE2 binding of VSVpp produced on HEK293T WT and *ATG5* KO cells as in (A) as assessed by a Spike-ACE2 interaction ELISA. recS, recombinant Spike. Bars represent the mean of $N = 3$ (independent experiments) ±SEM.

(D) Analysis of the infectivity of the particles produced in (A) by dividing the number of infected Caco-2 cells, either mock or Torin-1 (4 h, 0.5 μM) treated (S4E) with the amount of Spike (B). Infection was normalized to 100% for mock. Bars represent the mean of $N = 3$ (biological replicates) ±SEM.

(E) Infection of MRC5-ACE2 WT and *ATG5* KO cells with VSV(GFP)ΔG pseudoparticles produced in (A) containing the indicated proteins. Infected GFP+ cells were automatically quantified after 22 h post infection. Bars represent the mean of $N = 3$ (biological replicates) ±SEM. Student's t test with Welch's correction. *, $p < 0.05$; **, $p < 0.01$. ns (non-significant). n.d. (non-detectable).

autophagosome accumulation (Figure 6H). Taken together, these results suggest that E T9I interacts more strongly with components of autophagosome assembly machinery (SNX12, STX12, TMEM87B, and ABCG2) and that these interaction partners are required for E-mediated autophagosome accumulation.

DISCUSSION

The COVID-19 pandemic allowed unprecedented insights into the adaptation of zoonotic viruses to humans.[51,52] A study analyzing 6.4 million SARS-CoV-2 genomes revealed that the E T9I adaptation confers a transmission fitness advantage to Omicron.[15] Here, we show that the single adaptation E T9I is responsible for autophagy resistance of virions. Thus, our data suggest that autophagy manipulation by virion-associated E plays a significant role in SARS-CoV-2 transmission. Mechanistically, the Omicron-associated T9I mutation increases the localization of E to autophagosomes (Figure 4G) and promotes the recruitment of autophagosome-associated factors STX12, SNX12, TMEM87B, and ABCG2 (Figure 6H). All four cellular targets of E were not previously implicated in autophagy manipulation by viral pathogens and are endosome/lysosome-associated proteins.[48,53] STX12 and SNX12 are part of the Soluble *N*-ethylmaleimide sensitive factor attachment protein receptor complex and, together with SNAP29, mediate the fusion of autophagosomes with lysosomes.[46,54] This indicates that E T9I impairs the function of the fusion machinery to reduce autophagic flux.[55]

SARS-CoV-2 enters cells by both fusion at the plasma membrane and through the endosomal route[45,56,57], making incoming virions vulnerable to autophagy.[22,58,59] Interestingly, it was suggested that Omicron variants show increased entry via the endosomal route in some tissues and cell types.[60–62] It is thus tempting to speculate that E T9I promotes evasion of incoming virions by autophagy, enabling increased entry via the endosomal route.

It has previously been shown that, in addition to E, at least four other proteins encoded by SARS-CoV-2, including the nonstructural proteins Nsp15 and Nsp6, as well as open reading frame (ORF) 3a and ORF7a antagonize autophagy.[18,27,51] While Nsp15 reduces autophagic flux, Nsp6 exploits autophagy to

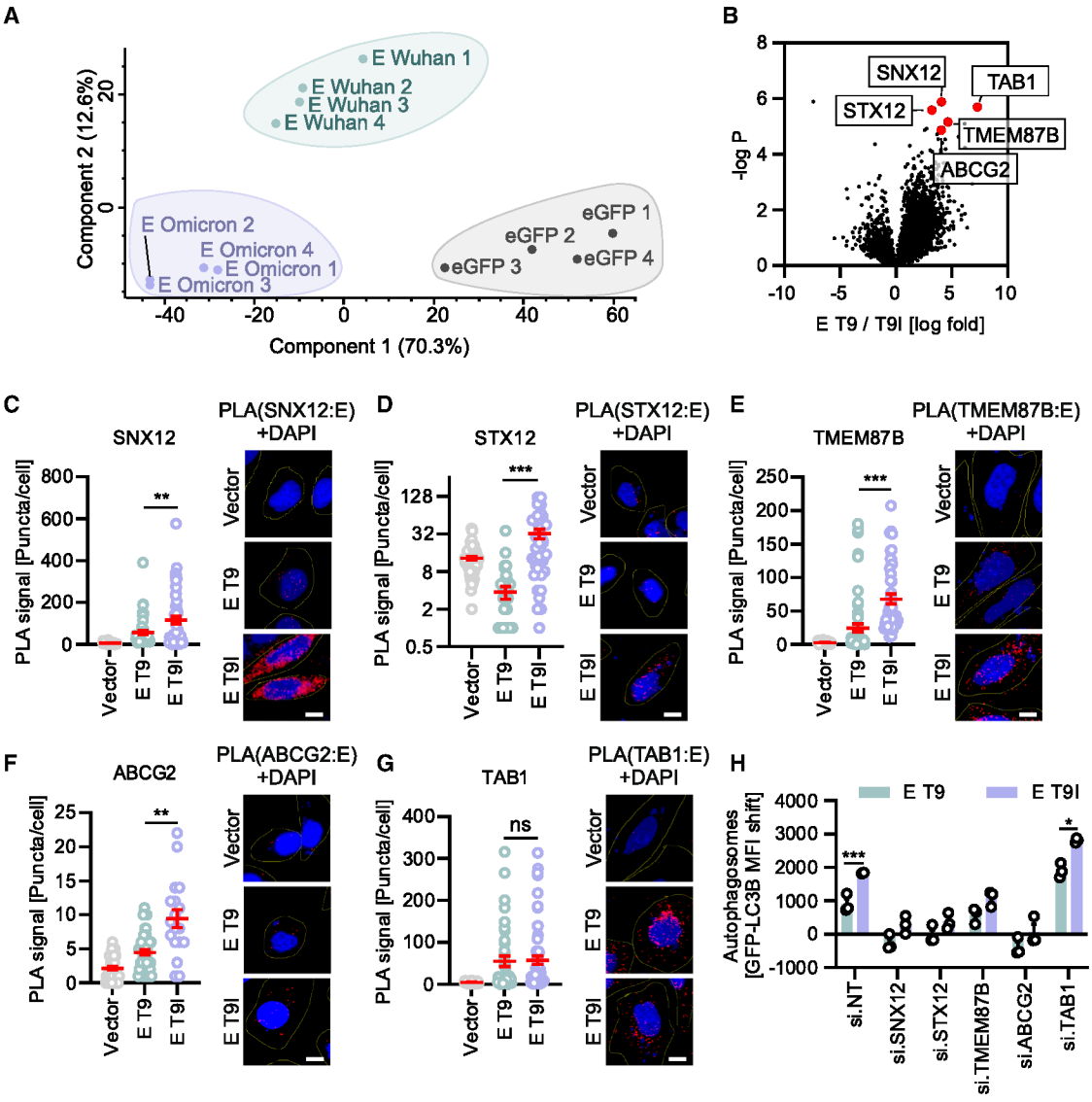

Figure 6. E T9I has increased affinity to autophagosome-associated proteins

(A) Principal component analysis of the differential interactome data (Data S1), the individual replicates are separated (black: GFP controls, Green: E T9 pulldown, Purple: E T9I pulldown) (B) Volcano plot of the differential interactome analysis showing enriched proteins in E T9I pulldown versus the *p* value (-log P). Five highly significantly enriched proteins are highlighted in red and via labels.

(C–G) Quantification of proximity ligation assays between transiently expressed SARS-CoV-2 E variants 30 h post transfection in HeLa cells and endogenous SNX12, STX12, TMEM87B, ABCG2 and TAB1, as indicated. Representative images depicted. PLA signal, red. Scale Bar, 10μm. DAPI, nuclei (blue). Lines represent the mean of $N = 18–59$ (individual cells) ±SEM.

(H) Quantification of autophagosome levels by flow cytometry in HEK293T autophagy reporter cells (HEK293T-GL) transiently expressing StrepII-tagged SARS-CoV-2 E variants (48 h post transfection) and depleted of indicated proteins by siRNA. Bars represent the mean of $N = 3$ (biological replicates) ±SEM. Student's *t* test with Welch's correction. *, $p < 0.05$; **, $p < 0.01$; ***, $p < 0.001$.

promote degradation of immune sensors.[18,63] Expression of the accessory proteins ORF3a and ORF7a resulted in the accumulation of non-acidified autophagosomes in the cytoplasm, indicating that they prevent autophagosome turnover.[18,64–67] While the Omicron-associated mutation T223I in ORF3a slightly increased its ability to inhibit autophagic flux, E T9I was the only variant that consistently outperformed its pre-Omicron version (Figure 2B). Notably, E is the only structural protein among the autophagy manipulating factors of SARS-CoV-2 and, hence, capable of protecting incoming virions. Therefore, E, ORF3a, ORF7a, Nsp6 and Nsp15 may cooperate to modulate autophagy at different steps of the SARS-CoV-2 replication cycle. In line with this, it has been reported that ORF3a exploits the autophagic machinery at a late stage to promote SARS-CoV-2 budding.[65] Other viruses may use similar strategies to promote virion stability. The M2 virion-associated membrane

pore protein of influenza A viruses also manipulates autophagy.[68] Similarly to M2, the function of E in autophagy was independent of its viroporin function (Figure S3A).

Adaptation to innate immune defenses emerges as a major contributing factor to the success of Omicron and the current transition of SARS-CoV-2 to endemic status.[1,20,69–71] Unlike humoral responses, innate immunity does not rapidly adapt to evolving virus variants.[72] Increased resistance toward autophagy may come at a cost - reduced replication fitness *in vitro* (Figure 3E). This may explain the delayed emergence of the E T9I mutation, despite its sporadic presence in pre-Omicron SARS-CoV-2 isolates.[38,39] It is tempting to speculate that E T9I contributed to the lower *in vitro* replication efficiency of early Omicron strains.[20,73,74] Of note, more recent Omicron subvariants exhibit increased replication speed *in vitro*, indicating the evolution of compensatory mutations.[6,74,75]

The immune system of bats, the reservoir species of SARS-CoV-2, is known to be highly tolerant to viruses without developing diseases.[76] Unlike other mammals, aging bats show increased levels of homeostatic autophagy.[77] Bat coronaviruses closely related to SARS-CoV-2 share a T in position 9 in E. Future analysis of differences between bat and human autophagy may improve our understanding of the evolution of autophagy and bats as a virus reservoir species.

In summary, our data show that the Omicron-associated T9I mutation in E mediates autophagy resistance and may contribute to the enhanced transmission fitness of Omicron. Thus, our study adds to the evidence that innate and adaptive immune evasion drove the evolution and success of Omicron *in vivo.*[13,20,69]

Limitations of the study

Our study primarily investigated the impact of the Omicron-associated T9I mutation in the E protein. This does not exclude the possibility that other Omicron-linked mutations, such as T223I in ORF3a, may also contribute to the variant's overall resistance to autophagy. However, only E, as a structural protein, may protect the incoming virion from autophagic degradation. The overall replication capacity of a variant reflects the combined effects of all its mutations. Mutations outside the E gene may therefore compensate for the replication defect caused by the T9I mutation in E. The potential impact of multiple mutations in recombinant viruses, however, was not addressed in this study. Although we identified interaction partners with increased binding affinity to E T9I, it remains unclear whether these partners are involved in the autophagic targeting of incoming capsids. Finally, it is yet to be determined whether E T9I also reduces viral growth while enhancing autophagy resistance in more complex systems, such as air-liquid interface lung cultures. Nevertheless, the notion that E T9I contributes to Omicron's overall fitness —and its continued presence in circulating SARS-CoV-2 variants as of May 2025— underscores its likely importance *in vivo*.

RESOURCE AVAILABILITY

Lead contact

Further information and requests for resources and reagents should be directed to and will be fulfilled by the lead contact, Konstantin Maria Johannes Sparrer (konstantin.sparrer@uni-ulm.de).

Materials availability

All unique reagents in this study are listed in the key resources table. Further information and requests for resources and reagents should be directed to and will be fulfilled by the lead contact.

Data and code availability

- All data reported in this paper will be shared by the lead contact upon request. The primary data is available via a Mendeley repository (Mendeley Data: https://doi.org/10.17632/6gbt6bnbrh.1, https://data.mendeley.com/datasets/6gbt6bnbrh/1). The mass spectrometry proteomics data have been deposited to the ProteomeXchange Consortium via the PRIDE partner repository (PRIDE: PXD048080, https://www.ebi.ac.uk/pride/archive/projects/PXD048080).
- This paper does not report original code.
- Any additional information required to reanalyze the data reported in this paper is available from the lead contact upon request.

ACKNOWLEDGMENTS

We thank Daniela Krnavek, Martha Mayer, Kerstin Regensburger, Regina Burger, Jana-Romana Fischer and Birgit Ott for assistance. We thank Prof. Alexander Kühne (Ulm University) for providing access to the Leica SP5 microscope (DFG project ID: 432000323). We thank Dr. Antonio Piras (TUM University) for analyzing proteomics samples. We thank Klaus Klumpp, Gary Ewart and Michelle Miller (Biotron Limited) for providing the SARS-CoV-2 E inhibitor BIT225. The SARS-CoV-2 variants, B.1.617.2 (Delta) and B.1.1.529 (Omicron BA.5), were kindly provided by Prof. Dr. Florian Schmidt and Dr. Bianca Schulte (University of Bonn, Bonn, Germany). K.M.J.S. acknowledges support from the German Ministry for Research and Education, now Federal Ministry of Research, Technology and Space (BMBF now BMFTR; IMMUNOMOD-01KI2014). This study was supported by the German Research Foundation (DFG) grants to K.M.J.S. (CRC1279-INST 40/623-1, SPP1923, SP 1600/6-1, SP 1600/7-1, SP1600/9-1), F.K. (CRC1279 and SPP1923), D.K. (KM 5/3-1), and A.P. (PI 1084/4, PI 1084/5 and TRR179/TP10, TRR237/A07, TRR353/B04). K.M.J.S. is additionally supported by the Baden-Wuerttemberg Stiftung (AutophagyBoost). Work in the A.P.'s laboratory was supported by an ERC Consolidator grant (ERC-CoG ProDAP), the Helmholtz Association's Initiative and Networking Fund (KA1-Co-02 "COVIPA"). D.K. is supported by a Baustein Grant from Ulm University, Else Kröner Fresenius Stiftung (2022_EKEA.47) and European Union's Horizon 2020 Marie Sklodowska-Curie program (No. 101062524). R.S., R.N., F.Z., and M.H. are supported by a Baustein Grant of Ulm University Medical Faculty (R.S.: L.SBN.0234; R.N.: L.SBN.0277; F.Z.: L.SBN.0225; M.H.: L.SBN.0245). S.K. and H.H. are part of the International Graduate School for Molecular Medicine, Ulm (IGradU). We further acknowledge the Bavarian State Ministry of Health, Bay-VOC (A.E.), IZKF Erlangen (Project A94) (A.E.) and the Bavarian Research Network FOR-COVID (A.P.).

AUTHOR CONTRIBUTIONS

S.K. performed the majority of the experimental work. R.N. performed all infectious SARS-CoV-2 experiments. A.C. and A.E. performed experiments with recombinant SARS-CoV-2. J.V. and A.P. performed and analyzed interactome studies. L.K. and H.H. generated expression constructs. C.J. and T. J. performed molecular modeling of SARS-CoV-2 E. M.H. took confocal fluorescence microscopy pictures and analyzed them. H.H. performed and analyzed proximity ligation assays. J-R.F. and F.Z. helped with pseudoparticle experiments. R.S. helped with experiments using lung cells. H.A., S. S., R.S-M., A.S.G-R., E.M.S., H.v.B., V.S., T.J., D.K., F.K., A.P., and A.E. provided resources and comments for the manuscript. K.M.J.S. conceived the study and wrote the manuscript. All authors reviewed and approved the manuscript.

DECLARATION OF INTERESTS

The authors declare no competing interests.

STAR★METHODS

Detailed methods are provided in the online version of this paper and include the following:

- KEY RESOURCES TABLE
- EXPERIMENTAL MODEL AND STUDY PARTICIPANT DETAILS
  - Cell culture
  - Study participant details
- METHOD DETAILS
  - Propagation of SARS-CoV-2
  - SARS-CoV-2 isolates
  - Generation and propagation of a rSARS-CoV-2
  - Analyzing growth of rSARS-CoV-2
  - Impact of autophagy on SARS-CoV-2 WT
  - TCID50 determination
  - siRNA-mediated knockdown
  - qRT-PCR
  - Impact of autophagy induction on IFITMs
  - Cloning and origin of expression constructs
  - Generation of VSV-pseudoparticles
  - VSV-pseudoparticle assays
  - Spike ELISA
  - Spike-ACE2 interaction assay
  - Autophagosome measurement by flow cytometry
  - Immunofluorescence microscopy
  - Cell viability analysis
  - Whole-cell and supernatant lysates
  - SDS-PAGE and immunoblotting
  - Co-immunoprecipitation
  - Proximity ligation assay (PLA)
  - Molecular modeling of SARS-CoV-2 E
  - Phylogenetic and mutation abundance analyses
  - Interactome studies of E-expressing cells
  - Data processing and analysis of MS
- QUANTIFICATION AND STATISTICAL ANALYSIS
  - Statistical analysis

SUPPLEMENTAL INFORMATION

Supplemental information can be found online at https://doi.org/10.1016/j.isci.2025.112974.

Received: August 29, 2024
Revised: April 3, 2025
Accepted: June 18, 2025
Published: June 20, 2025

REFERENCES

1. Steiner, S., Kratzel, A., Barut, G.T., Lang, R.M., Aguiar Moreira, E., Thomann, L., Kelly, J.N., and Thiel, V. (2024). SARS-CoV-2 biology and host interactions. Nat. Rev. Microbiol. *22*, 206–225. https://doi.org/10.1038/s41579-023-01003-z.
2. V'kovski, P., Kratzel, A., Steiner, S., Stalder, H., and Thiel, V. (2021). Coronavirus biology and replication: implications for SARS-CoV-2. Nat. Rev. Microbiol. *19*, 155–170. https://doi.org/10.1038/s41579-020-00468-6.
3. Carabelli, A.M., Peacock, T.P., Thorne, L.G., Harvey, W.T., Hughes, J., COVID-19 Genomics UK Consortium; Peacock, S.J., Barclay, W.S., de Silva, T.I., Towers, G.J., and Robertson, D.L. (2023). SARS-CoV-2 variant biology: immune escape, transmission and fitness. Nat. Rev. Microbiol. *21*, 162–177. https://doi.org/10.1038/s41579-022-00841-7.
4. Fan, Y., Li, X., Zhang, L., Wan, S., Zhang, L., and Zhou, F. (2022). SARS-CoV-2 Omicron variant: recent progress and future perspectives. Sig. Transduct. Target. Ther. *7*, 141. https://doi.org/10.1038/s41392-022-00997-x.
5. Cao, Y., Wang, J., Jian, F., Xiao, T., Song, W., Yisimayi, A., Huang, W., Li, Q., Wang, P., An, R., et al. (2022). Omicron escapes the majority of existing SARS-CoV-2 neutralizing antibodies. Nature *602*, 657–663. https://doi.org/10.1038/s41586-021-04385-3.
6. Hoffmann, M., Wong, L.-Y.R., Arora, P., Zhang, L., Rocha, C., Odle, A., Nehlmeier, I., Kempf, A., Richter, A., Halwe, N.J., et al. (2023). Omicron subvariant BA.5 efficiently infects lung cells. Nat. Commun. *14*, 3500. https://doi.org/10.1038/s41467-023-39147-4.
7. Willett, B.J., Grove, J., MacLean, O.A., Wilkie, C., De Lorenzo, G., Furnon, W., Cantoni, D., Scott, S., Logan, N., Ashraf, S., et al. (2022). SARS-CoV-2 Omicron is an immune escape variant with an altered cell entry pathway. Nat. Microbiol. *7*, 1161–1179. https://doi.org/10.1038/s41564-022-01143-7.
8. Viana, R., Moyo, S., Amoako, D.G., Tegally, H., Scheepers, C., Althaus, C. L., Anyaneji, U.J., Bester, P.A., Boni, M.F., Chand, M., et al. (2022). Rapid epidemic expansion of the SARS-CoV-2 Omicron variant in southern Africa. Nature *603*, 679–686. https://doi.org/10.1038/s41586-022-04411-y.
9. Kaku, Y., Okumura, K., Padilla-Blanco, M., Kosugi, Y., Uriu, K., Hinay, A. A., Chen, L., Plianchaisuk, A., Kobiyama, K., Ishii, K.J., et al. (2024). Virological characteristics of the SARS-CoV-2 JN.1 variant. Lancet Infect. Dis. *24*, e82. https://doi.org/10.1016/S1473-3099(23)00813-7.
10. Kaku, Y., Yo, M.S., Tolentino, J.E., Uriu, K., Okumura, K., Genotype to Phenotype Japan G2P-Japan Consortium; Ito, J., and Sato, K. (2024). Virological characteristics of the SARS-CoV-2 KP.3, LB.1, and KP.2.3 variants. Lancet Infect. Dis. *24*, e482–e483. https://doi.org/10.1016/S1473-3099(24)00415-8.
11. Jung, C., Kmiec, D., Koepke, L., Zech, F., Jacob, T., Sparrer, K.M.J., and Kirchhoff, F. (2022). Omicron: what makes the latest SARS-CoV-2 variant of concern so concerning? J. Virol. *96*, e0207721. https://doi.org/10.1128/jvi.02077-21.
12. Planas, D., Veyer, D., Baidaliuk, A., Staropoli, I., Guivel-Benhassine, F., Rajah, M.M., Planchais, C., Porrot, F., Robillard, N., Puech, J., et al. (2021). Reduced sensitivity of SARS-CoV-2 variant Delta to antibody neutralization. Nature *596*, 276–280. https://doi.org/10.1038/s41586-021-03777-9.
13. Planas, D., Saunders, N., Maes, P., Guivel-Benhassine, F., Planchais, C., Buchrieser, J., Bolland, W.-H., Porrot, F., Staropoli, I., Lemoine, F., et al. (2022). Considerable escape of SARS-CoV-2 Omicron to antibody neutralization. Nature *602*, 671–675. https://doi.org/10.1038/s41586-021-04389-z.
14. Pastorio, C., Zech, F., Noettger, S., Jung, C., Jacob, T., Sanderson, T., Sparrer, K.M.J., and Kirchhoff, F. (2022). Determinants of Spike infectivity, processing, and neutralization in SARS-CoV-2 Omicron subvariants BA.1 and BA.2. Cell Host Microbe *30*, 1255–1268.e5. https://doi.org/10.1016/j.chom.2022.07.006.
15. Obermeyer, F., Jankowiak, M., Barkas, N., Schaffner, S.F., Pyle, J.D., Yurkovetskiy, L., Bosso, M., Park, D.J., Babadi, M., MacInnis, B.L., et al. (2022). Analysis of 6.4 million SARS-CoV-2 genomes identifies mutations associated with fitness. Science *376*, 1327–1332. https://doi.org/10.1126/science.abm1208.
16. Stukalov, A., Girault, V., Grass, V., Karayel, O., Bergant, V., Urban, C., Haas, D.A., Huang, Y., Oubraham, L., Wang, A., et al. (2021). Multilevel proteomics reveals host perturbations by SARS-CoV-2 and SARS-CoV. Nature *594*, 246–252. https://doi.org/10.1038/s41586-021-03493-4.
17. Gassen, N.C., Papies, J., Bajaj, T., Emanuel, J., Dethloff, F., Chua, R.L., Trimpert, J., Heinemann, N., Niemeyer, C., Weege, F., et al. (2021). SARS-CoV-2-mediated dysregulation of metabolism and autophagy uncovers host-targeting antivirals. Nat. Commun. *12*, 3818. https://doi.org/10.1038/s41467-021-24007-w.
18. Hayn, M., Hirschenberger, M., Koepke, L., Nchioua, R., Straub, J.H., Klute, S., Hunszinger, V., Zech, F., Prelli Bozzo, C., Aftab, W., et al. (2021). Systematic functional analysis of SARS-CoV-2 proteins uncovers viral innate immune antagonists and remaining vulnerabilities. Cell Rep. *35*, 109126. https://doi.org/10.1016/j.celrep.2021.109126.

19. Nchioua, R., Kmiec, D., Müller, J.A., Conzelmann, C., Groß, R., Swanson, C.M., Neil, S.J.D., Stenger, S., Sauter, D., Münch, J., et al. (2020). SARS-CoV-2 Is Restricted by Zinc Finger Antiviral Protein despite Preadaptation to the Low-CpG Environment in Humans. mBio *11*, 10. https://doi.org/10.1128/mBio.01930-20.

20. Nchioua, R., Schundner, A., Klute, S., Koepke, L., Hirschenberger, M., Noettger, S., Fois, G., Zech, F., Graf, A., Krebs, S., et al. (2023). Reduced replication but increased interferon resistance of SARS-CoV-2 Omicron BA.1. Life Sci. Alliance *6*, e202201745. https://doi.org/10.26508/lsa.202201745.

21. Levine, B., Mizushima, N., and Virgin, H.W. (2011). Autophagy in immunity and inflammation. Nature *469*, 323–335. https://doi.org/10.1038/nature09782.

22. Choi, Y., Bowman, J.W., and Jung, J.U. (2018). Autophagy during viral infection - a double-edged sword. Nat. Rev. Microbiol. *16*, 341–354. https://doi.org/10.1038/s41579-018-0003-6.

23. He, C., and Klionsky, D.J. (2009). Regulation mechanisms and signaling pathways of autophagy. Annu. Rev. Genet. *43*, 67–93. https://doi.org/10.1146/annurev-genet-102808-114910.

24. Klute, S., and Sparrer, K.M.J. (2024). Friends and Foes: The Ambivalent Role of Autophagy in HIV-1 Infection. Viruses *16*, 500. https://doi.org/10.3390/v16040500.

25. Feng, Y., He, D., Yao, Z., and Klionsky, D.J. (2014). The machinery of macroautophagy. Cell Res. *24*, 24–41. https://doi.org/10.1038/cr.2013.168.

26. Gatica, D., Lahiri, V., and Klionsky, D.J. (2018). Cargo recognition and degradation by selective autophagy. Nat. Cell Biol. *20*, 233–242. https://doi.org/10.1038/s41556-018-0037-z.

27. Koepke, L., Hirschenberger, M., Hayn, M., Kirchhoff, F., and Sparrer, K.M. (2021). Manipulation of autophagy by SARS-CoV-2 proteins. Autophagy *17*, 2659–2661. https://doi.org/10.1080/15548627.2021.1953847.

28. Boson, B., Legros, V., Zhou, B., Siret, E., Mathieu, C., Cosset, F.-L., Lavillette, D., and Denolly, S. (2021). The SARS-CoV-2 envelope and membrane proteins modulate maturation and retention of the spike protein, allowing assembly of virus-like particles. J. Biol. Chem. *296*, 100111. https://doi.org/10.1074/jbc.RA120.016175.

29. Chai, J., Cai, Y., Pang, C., Wang, L., McSweeney, S., Shanklin, J., and Liu, Q. (2021). Structural basis for SARS-CoV-2 envelope protein recognition of human cell junction protein PALS1. Nat. Commun. *12*, 3433. https://doi.org/10.1038/s41467-021-23533-x.

30. Zhou, S., Lv, P., Li, M., Chen, Z., Xin, H., Reilly, S., and Zhang, X. (2023). SARS-CoV-2 E protein: Pathogenesis and potential therapeutic development. Biomed. Pharmacother. *159*, 114242. https://doi.org/10.1016/j.biopha.2023.114242.

31. Wang, W.-A., Carreras-Sureda, A., and Demaurex, N. (2023). SARS-CoV-2 infection alkalinizes the ERGIC and lysosomes through the viroporin activity of the viral envelope protein. J. Cell Sci. *136*, jcs260685. https://doi.org/10.1242/jcs.260685.

32. Kim, Y.C., and Guan, K.-L. (2015). mTOR: a pharmacologic target for autophagy regulation. J. Clin. Investig. *125*, 25–32. https://doi.org/10.1172/JCI73939.

33. Shi, G., Chiramel, A.I., Li, T., Lai, K.K., Kenney, A.D., Zani, A., Eddy, A.C., Majdoul, S., Zhang, L., Dempsey, T., et al. (2022). Rapalogs downmodulate intrinsic immunity and promote cell entry of SARS-CoV-2. J. Clin. Investig. *132*, e160766. https://doi.org/10.1172/JCI160766.

34. Koepke, L., Winter, B., Grenzner, A., Regensburger, K., Engelhart, S., van der Merwe, J.A., Krebs, S., Blum, H., Kirchhoff, F., and Sparrer, K.M.J. (2020). An improved method for high-throughput quantification of autophagy in mammalian cells. Sci. Rep. *10*, 12241. https://doi.org/10.1038/s41598-020-68607-w.

35. Klionsky, D.J., Abdel-Aziz, A.K., Abdelfatah, S., Abdellatif, M., Abdoli, A., Abel, S., Abeliovich, H., Abildgaard, M.H., Abudu, Y.P., Acevedo-Arozena, A., et al. (2021). Guidelines for the use and interpretation of assays for monitoring autophagy (4th edition)1. Autophagy *17*, 1–382. https://doi.org/10.1080/15548627.2020.1797280.

36. Chen, C., Nadeau, S., Yared, M., Voinov, P., Xie, N., Roemer, C., and Stadler, T. (2022). CoV-Spectrum: analysis of globally shared SARS-CoV-2 data to identify and characterize new variants. Bioinformatics *38*, 1735–1737. https://doi.org/10.1093/bioinformatics/btab856.

37. Carreño, J.M., Alshammary, H., Tcheou, J., Singh, G., Raskin, A.J., Kawabata, H., Sominsky, L.A., Clark, J.J., Adelsberg, D.C., Bielak, D.A., et al. (2022). Activity of convalescent and vaccine serum against SARS-CoV-2 Omicron. Nature *602*, 682–688. https://doi.org/10.1038/s41586-022-04399-5.

38. Gonzalez-Reiche, A.S., Hernandez, M.M., Sullivan, M.J., Ciferri, B., Alshammary, H., Obla, A., Fabre, S., Kleiner, G., Polanco, J., Khan, Z., et al. (2020). Introductions and early spread of SARS-CoV-2 in the New York City area. Science *369*, 297–301. https://doi.org/10.1126/science.abc1917.

39. Gonzalez-Reiche, A.S., Alshammary, H., Schaefer, S., Patel, G., Polanco, J., Carreño, J.M., Amoako, A.A., Rooker, A., Cognigni, C., Floda, D., et al. (2023). Sequential intrahost evolution and onward transmission of SARS-CoV-2 variants. Nat. Commun. *14*, 3235. https://doi.org/10.1038/s41467-023-38867-x.

40. Herrmann, A., Jungnickl, D., Cordsmeier, A., Peter, A.S., Überla, K., and Ensser, A. (2021). Cloning of a Passage-Free SARS-CoV-2 Genome and Mutagenesis Using Red Recombination. Int. J. Mol. Sci. *22*, 10188. https://doi.org/10.3390/ijms221910188.

41. Medeiros-Silva, J., Dregni, A.J., Somberg, N.H., Duan, P., and Hong, M. (2023). Atomic structure of the open SARS-CoV-2 E viroporin. Sci. Adv. *9*, eadi9007. https://doi.org/10.1126/sciadv.adi9007.

42. Ewart, G., Bobardt, M., Bentzen, B.H., Yan, Y., Thomson, A., Klumpp, K., Becker, S., Rosenkilde, M.M., Miller, M., and Gallay, P. (2023). Post-infection treatment with the E protein inhibitor BIT225 reduces disease severity and increases survival of K18-hACE2 transgenic mice infected with a lethal dose of SARS-CoV-2. PLoS Pathog. *19*, e1011328. https://doi.org/10.1371/journal.ppat.1011328.

43. Kudchodkar, S.B., and Levine, B. (2009). Viruses and autophagy. Rev. Med. Virol. *19*, 359–378. https://doi.org/10.1002/rmv.630.

44. Zech, F., Schniertshauer, D., Jung, C., Herrmann, A., Cordsmeier, A., Xie, Q., Nchioua, R., Prelli Bozzo, C., Volcic, M., Koepke, L., et al. (2021). Spike residue 403 affects binding of coronavirus spikes to human ACE2. Nat. Commun. *12*, 6855. https://doi.org/10.1038/s41467-021-27180-0.

45. Hoffmann, M., Kleine-Weber, H., Schroeder, S., Krüger, N., Herrler, T., Erichsen, S., Schiergens, T.S., Herrler, G., Wu, N.-H., Nitsche, A., et al. (2020). SARS-CoV-2 Cell Entry Depends on ACE2 and TMPRSS2 and Is Blocked by a Clinically Proven Protease Inhibitor. Cell *181*, 271–280.e8. https://doi.org/10.1016/j.cell.2020.02.052.

46. Morelli, E., Ginefra, P., Mastrodonato, V., Beznoussenko, G.V., Rusten, T.E., Bilder, D., Stenmark, H., Mironov, A.A., and Vaccari, T. (2014). Multiple functions of the SNARE protein Snap29 in autophagy, endocytic, and exocytic trafficking during epithelial formation in Drosophila. Autophagy *10*, 2251–2268. https://doi.org/10.4161/15548627.2014.981913.

47. Lenoir, M., Ustunel, C., Rajesh, S., Kaur, J., Moreau, D., Gruenberg, J., and Overduin, M. (2018). Phosphorylation of conserved phosphoinositide binding pocket regulates sorting nexin membrane targeting. Nat. Commun. *9*, 993. https://doi.org/10.1038/s41467-018-03370-1.

48. Hirata, T., Fujita, M., Nakamura, S., Gotoh, K., Motooka, D., Murakami, Y., Maeda, Y., and Kinoshita, T. (2015). Post-Golgi anterograde transport requires GARP-dependent endosome-to-TGN retrograde transport. Mol. Biol. Cell *26*, 3071–3084. https://doi.org/10.1091/mbc.E14-11-1568.

49. Yin, W., Xiang, D., Wang, T., Zhang, Y., Pham, C.V., Zhou, S., Jiang, G., Hou, Y., Zhu, Y., Han, Y., et al. (2021). The inhibition of ABCB1/MDR1 or ABCG2/BCRP enables doxorubicin to eliminate liver cancer stem cells. Sci. Rep. *11*, 10791. https://doi.org/10.1038/s41598-021-89931-9.

50. Criollo, A., Niso-Santano, M., Malik, S.A., Michaud, M., Morselli, E., Mariño, G., Lachkar, S., Arkhipenko, A.V., Harper, F., Pierron, G., et al. (2011). Inhibition of autophagy by TAB2 and TAB3. EMBO J. *30*, 4908–4920. https://doi.org/10.1038/emboj.2011.413.

51. Hoenigsperger, H., Sivarajan, R., and Sparrer, K.M. (2024). Differences and similarities between innate immune evasion strategies of human coronaviruses. Curr. Opin. Microbiol. *79*, 102466. https://doi.org/10.1016/j.mib.2024.102466.

52. Markov, P.V., Ghafari, M., Beer, M., Lythgoe, K., Simmonds, P., Stilianakis, N.I., and Katzourakis, A. (2023). The evolution of SARS-CoV-2. Nat. Rev. Microbiol. *21*, 361–379. https://doi.org/10.1038/s41579-023-00878-2.

53. Mózner, O., Bartos, Z., Zámbó, B., Homolya, L., Hegedűs, T., and Sarkadi, B. (2019). Cellular Processing of the ABCG2 Transporter—Potential Effects on Gout and Drug Metabolism. Cells *8*, 1215. https://doi.org/10.3390/cells8101215.

54. Tang, Q., Gao, P., Arzberger, T., Höllerhage, M., Herms, J., Höglinger, G., and Koeglsperger, T. (2021). Alpha-Synuclein defects autophagy by impairing SNAP29-mediated autophagosome-lysosome fusion. Cell Death Dis. *12*, 854. https://doi.org/10.1038/s41419-021-04138-0.

55. Lőrincz, P., and Juhász, G. (2020). Autophagosome-Lysosome Fusion. J. Mol. Biol. *432*, 2462–2482. https://doi.org/10.1016/j.jmb.2019.10.028.

56. Jackson, C.B., Farzan, M., Chen, B., and Choe, H. (2022). Mechanisms of SARS-CoV-2 entry into cells. Nat. Rev. Mol. Cell Biol. *23*, 3–20. https://doi.org/10.1038/s41580-021-00418-x.

57. Prelli Bozzo, C., Nchioua, R., Volcic, M., Koepke, L., Krüger, J., Schütz, D., Heller, S., Stürzel, C.M., Kmiec, D., Conzelmann, C., et al. (2021). IFITM proteins promote SARS-CoV-2 infection and are targets for virus inhibition in vitro. Nat. Commun. *12*, 4584. https://doi.org/10.1038/s41467-021-24817-y.

58. Jassey, A., and Jackson, W.T. (2024). Viruses and autophagy: bend, but don't break. Nat. Rev. Microbiol. *22*, 309–321. https://doi.org/10.1038/s41579-023-00995-y.

59. Tooze, S.A., Abada, A., and Elazar, Z. (2014). Endocytosis and Autophagy: Exploitation or Cooperation? Cold Spring Harb. Perspect. Biol. *6*, a018358. https://doi.org/10.1101/cshperspect.a018358.

60. Du, X., Tang, H., Gao, L., Wu, Z., Meng, F., Yan, R., Qiao, S., An, J., Wang, C., and Qin, F.X.-F. (2022). Omicron adopts a different strategy from Delta and other variants to adapt to host. Sig Transduct Target Ther *7*, 45. https://doi.org/10.1038/s41392-022-00903-5.

61. Zhao, H., Lu, L., Peng, Z., Chen, L.-L., Meng, X., Zhang, C., Ip, J.D., Chan, W.-M., Chu, A.W.-H., Chan, K.-H., et al. (2022). SARS-CoV-2 Omicron variant shows less efficient replication and fusion activity when compared with Delta variant in TMPRSS2-expressed cells. Emerg. Microbes Infect. *11*, 277–283. https://doi.org/10.1080/22221751.2021.2023329.

62. Hoffmann, M., Krüger, N., Schulz, S., Cossmann, A., Rocha, C., Kempf, A., Nehlmeier, I., Graichen, L., Moldenhauer, A.-S., Winkler, M.S., et al. (2022). The Omicron variant is highly resistant against antibody-mediated neutralization: Implications for control of the COVID-19 pandemic. Cell *185*, 447–456.e11. https://doi.org/10.1016/j.cell.2021.12.032.

63. Jiao, P., Fan, W., Ma, X., Lin, R., Zhao, Y., Li, Y., Zhang, H., Jia, X., Bi, Y., Feng, X., et al. (2023). SARS-CoV-2 nonstructural protein 6 triggers endoplasmic reticulum stress-induced autophagy to degrade STING1. Autophagy *19*, 3113–3131. https://doi.org/10.1080/15548627.2023.2238579.

64. Zhang, Y., Sun, H., Pei, R., Mao, B., Zhao, Z., Li, H., Lin, Y., and Lu, K. (2021). The SARS-CoV-2 protein ORF3a inhibits fusion of autophagosomes with lysosomes. Cell Discov. *7*, 31. https://doi.org/10.1038/s41421-021-00268-z.

65. Chen, D., Zheng, Q., Sun, L., Ji, M., Li, Y., Deng, H., and Zhang, H. (2021). ORF3a of SARS-CoV-2 promotes lysosomal exocytosis-mediated viral egress. Dev. Cell *56*, 3250–3263.e5. https://doi.org/10.1016/j.devcel.2021.10.006.

66. Miao, G., Zhao, H., Li, Y., Ji, M., Chen, Y., Shi, Y., Bi, Y., Wang, P., and Zhang, H. (2021). ORF3a of the COVID-19 virus SARS-CoV-2 blocks HOPS complex-mediated assembly of the SNARE complex required for autolysosome formation. Dev. Cell *56*, 427–442.e5. https://doi.org/10.1016/j.devcel.2020.12.010.

67. Hou, P., Wang, X., Wang, H., Wang, T., Yu, Z., Xu, C., Zhao, Y., Wang, W., Zhao, Y., Chu, F., et al. (2023). The ORF7a protein of SARS-CoV-2 initiates autophagy and limits autophagosome-lysosome fusion via degradation of SNAP29 to promote virus replication. Autophagy *19*, 551–569. https://doi.org/10.1080/15548627.2022.2084686.

68. Beale, R., Wise, H., Stuart, A., Ravenhill, B.J., Digard, P., and Randow, F. (2014). A LC3-interacting motif in the influenza A virus M2 protein is required to subvert autophagy and maintain virion stability. Cell Host Microbe *15*, 239–247. https://doi.org/10.1016/j.chom.2014.01.006.

69. Guo, K., Barrett, B.S., Morrison, J.H., Mickens, K.L., Vladar, E.K., Hasenkrug, K.J., Poeschla, E.M., and Santiago, M.L. (2022). Interferon resistance of emerging SARS-CoV-2 variants. Proc. Natl. Acad. Sci. USA *119*, e2203760119. https://doi.org/10.1073/pnas.2203760119.

70. Tao, K., Tzou, P.L., Nouhin, J., Gupta, R.K., de Oliveira, T., Kosakovsky Pond, S.L., Fera, D., and Shafer, R.W. (2021). The biological and clinical significance of emerging SARS-CoV-2 variants. Nat. Rev. Genet. *22*, 757–773. https://doi.org/10.1038/s41576-021-00408-x.

71. Nesteruk, I. (2023). Endemic characteristics of SARS-CoV-2 infection. Sci. Rep. *13*, 14841. https://doi.org/10.1038/s41598-023-41841-8.

72. Akira, S., Uematsu, S., and Takeuchi, O. (2006). Pathogen recognition and innate immunity. Cell *124*, 783–801. https://doi.org/10.1016/j.cell.2006.02.015.

73. Harvey, W.T., Carabelli, A.M., Jackson, B., Gupta, R.K., Thomson, E.C., Harrison, E.M., Ludden, C., Reeve, R., Rambaut, A., et al.; COVID-19 Genomics UK COG-UK Consortium (2021). SARS-CoV-2 variants, spike mutations and immune escape. Nat. Rev. Microbiol. *19*, 409–424. https://doi.org/10.1038/s41579-021-00573-0.

74. Nchioua, R., Diofano, F., Noettger, S., von Maltitz, P., Stenger, S., Zech, F., Münch, J., Sparrer, K.M.J., Just, S., and Kirchhoff, F. (2022). Strong attenuation of SARS-CoV-2 Omicron BA.1 and increased replication of the BA.5 subvariant in human cardiomyocytes. Signal Transduct. Target. Ther. *7*, 395. https://doi.org/10.1038/s41392-022-01256-9.

75. Kimura, I., Yamasoba, D., Tamura, T., Nao, N., Suzuki, T., Oda, Y., Mitoma, S., Ito, J., Nasser, H., Zahradnik, J., et al. (2022). Virological characteristics of the SARS-CoV-2 Omicron BA.2 subvariants, including BA.4 and BA.5. Cell *185*, 3992–4007.e16. https://doi.org/10.1016/j.cell.2022.09.018.

76. Irving, A.T., Ahn, M., Goh, G., Anderson, D.E., and Wang, L.-F. (2021). Lessons from the host defences of bats, a unique viral reservoir. Nature *589*, 363–370. https://doi.org/10.1038/s41586-020-03128-0.

77. Kacprzyk, J., Locatelli, A.G., Hughes, G.M., Huang, Z., Clarke, M., Gorbunova, V., Sacchi, C., Stewart, G.S., and Teeling, E.C. (2021). Evolution of mammalian longevity: age-related increase in autophagy in bats compared to other mammals. Aging (Albany NY) *13*, 7998–8025. https://doi.org/10.18632/aging.202852.

78. Gordon, D.E., Jang, G.M., Bouhaddou, M., Xu, J., Obernier, K., White, K.M., O'Meara, M.J., Rezelj, V.V., Guo, J.Z., Swaney, D.L., et al. (2020). A SARS-CoV-2 protein interaction map reveals targets for drug repurposing. Nature *583*, 459–468. https://doi.org/10.1038/s41586-020-2286-9.

79. Hoenigsperger, H., Koepke, L., Acharya, D., Hunszinger, V., Freisem, D., Grenzner, A., Wiese, S., Kirchhoff, F., Gack, M.U., and Sparrer, K.M.J. (2024). CSNK2 suppresses autophagy by activating FLN-NHL-containing TRIM proteins. Autophagy *20*, 994–1014. https://doi.org/10.1080/15548627.2023.2281128.

80. Humphrey, W., Dalke, A., and Schulten, K. (1996). VMD: visual molecular dynamics. J. Mol. Graph. *14*, 33. https://doi.org/10.1016/0263-7855(96)00018-5.

81. Cordsmeier, A., Jungnickl, D., Herrmann, A., Korn, K., and Ensser, A. (2023). Analysis of SARS-CoV-2 Spike Protein Variants with Recombinant

Reporter Viruses Created from a Bacmid System. Int. J. Mol. Sci. *24*, 8156. https://doi.org/10.3390/ijms24098156.

82. REED, L.J., and MUENCH, H. (1938). A SIMPLE METHOD OF ESTIMATING FIFTY PER CENT ENDPOINTS12. Am. J. Epidemiol. *27*, 493–497. https://doi.org/10.1093/oxfordjournals.aje.a118408.
83. Acharya, D., Reis, R., Volcic, M., Liu, G., Wang, M.K., Chia, B.S., Nchioua, R., Groß, R., Münch, J., Kirchhoff, F., et al. (2022). Actin cytoskeleton remodeling primes RIG-I-like receptor activation. Cell *185*, 3588–3602. e21. https://doi.org/10.1016/j.cell.2022.08.011.
84. Volcic, M., Sparrer, K.M.J., Koepke, L., Hotter, D., Sauter, D., Stürzel, C. M., Scherer, M., Stamminger, T., Hofmann, T.G., Arhel, N.J., et al. (2020). Vpu modulates DNA repair to suppress innate sensing and hyper-integration of HIV-1. Nat. Microbiol. *5*, 1247–1261. https://doi.org/10.1038/s41564-020-0753-6.
85. Chenoweth, K., van Duin, A.C.T., and Goddard, W.A. (2008). ReaxFF reactive force field for molecular dynamics simulations of hydrocarbon oxidation. J. Phys. Chem. A *112*, 1040–1053. https://doi.org/10.1021/jp709896w.
86. Smart, O.S., Neduvelil, J.G., Wang, X., Wallace, B.A., and Sansom, M.S. (1996). HOLE: a program for the analysis of the pore dimensions of ion channel structural models. J. Mol. Graph. *14*, 354–376. https://doi.org/10.1016/s0263-7855(97)00009-x.
87. Hadfield, J., Megill, C., Bell, S.M., Huddleston, J., Potter, B., Callender, C., Sagulenko, P., Bedford, T., and Neher, R.A. (2018). Nextstrain: real-time tracking of pathogen evolution. Bioinformatics *34*, 4121–4123. https://doi.org/10.1093/bioinformatics/bty407.
88. Sagulenko, P., Puller, V., and Neher, R.A. (2018). TreeTime: Maximum-likelihood phylodynamic analysis. Virus Evol. *4*, vex042. https://doi.org/10.1093/ve/vex042.
89. Tyanova, S., Temu, T., and Cox, J. (2016). The MaxQuant computational platform for mass spectrometry-based shotgun proteomics. Nat. Protoc. *11*, 2301–2319. https://doi.org/10.1038/nprot.2016.136.
90. Tyanova, S., Temu, T., Sinitcyn, P., Carlson, A., Hein, M.Y., Geiger, T., Mann, M., and Cox, J. (2016). The Perseus computational platform for comprehensive analysis of (prote)omics data. Nat. Methods *13*, 731–740. https://doi.org/10.1038/nmeth.3901.

STAR★METHODS

KEY RESOURCES TABLE

REAGENT or RESOURCE	SOURCE	IDENTIFIER
Antibodies		
Goat anti-Mouse IgG (H + L) Highly Cross-Adsorbed Secondary Antibody, AF568 (IF 1:400)	Thermo Scientific	Cat#A11004; RRID: AB_2534072
Goat anti-Rabbit IgG (H + L) Highly Cross-Adsorbed Secondary Antibody, AF647 (IF 1:400)	Thermo Scientific	Cat#A21245; RRID: AB_2535813
Goat anti-Rabbit IgG H&L (HRP) Secondary Antibody (WB:1:10,000)	Abcam	Cat#ab6721; RRID: AB_955447
IRDye 680RD Goat anti-Rabbit IgG Secondary Antibody (WB 1:20,000)	LI-COR	Cat#926–68071; RRID: AB_10956166
IRDye 680RD Goat anti-Rat IgG Secondary Antibody (WB 1:20,000)	LI-COR	Cat#926–68076; RRID: AB_10956590
IRDye 800CW Goat anti-Mouse IgG Secondary Antibody (WB 1:20,000)	LI-COR	Cat#926–32210; RRID: AB_621842
IRDye 800CW Goat anti-Rat IgG Secondary Antibody (WB 1:20,000)	LI-COR	Cat#926–32219; RRID: AB_1850025
Monoclonal mouse anti-ABCG2 Antibody (BXP-21) (PLA 1:100)	Santa Cruz Biotechnology	Cat#sc-58222; RRID: AB_630828
Monoclonal mouse anti-β-actin Antibody (AC-15) (WB 1:10,000)	Sigma-Aldrich	Cat#A5441; RRID: AB_476744
Monoclonal mouse anti-p62 Antibody (2C11) (WB 1:1,000)	Abcam	Cat#ab56416; RRID: AB_945626
Monoclonal mouse anti-StrepII-tag Antibody (517) (IF 1:200; PLA 1:450)	Novus Biologicals	Cat#NBP2-43735
Monoclonal mouse anti-V5 Antibody (E9H80) (WB 1:3,000; Spike-ACE2 interaction assay 1:1,000)	Cell Signaling Technology	Cat#80076; RRID: AB_2920661
Monoclonal mouse anti-VSV-M Antibody (23H12) (WB 1:5,000)	Kerafast	Cat#EB0011; RRID: AB_2734773
Monoclonal rabbit anti-ABCG2 Antibody (2K8X1) (WB 1:500)	Novus Biologicals	Cat#NBP3-15559
Monoclonal rabbit anti-IFITM3 Antibody (D8E8G) (WB 1:500)	Cell Signaling Technology	Cat#59212; RRID: AB_2799561
Monoclonal rabbit anti-LAMP1 Antibody (D2D11) (IF 1:200)	Cell Signaling Technology	Cat#9091S; RRID: AB_2687579
Monoclonal rabbit anti-Rab7 Antibody (EPR7589) (IF 1:500)	Abcam	Cat#ab137029; RRID: AB_2629474
Monoclonal rat anti-GAPDH Antibody (W17079A) (WB 1:1,000)	BioLegend	Cat#607902; RRID: AB_2734503
Normal Rabbit IgG Polyclonal Antibody control (IP)	Sigma-Aldrich	Cat#12-370
Polyclonal rabbit anti-ABCG2 Antibody (IP)	Cell Signaling Technology	Cat#4477S; RRID: AB 10544928
Polyclonal rabbit anti-IFITM1 Antibody (WB 1:500)	Cell Signaling Technology	Cat#13126; RRID: AB_2798126
Polyclonal rabbit anti-IFITM2 Antibody (WB 1:500)	Abcam	Cat#ab236735
Polyclonal rabbit anti-LC3 Antibody (WB 1:200)	Sigma-Aldrich	Cat#L8918; RRID: AB_1079382

(*Continued on next page*)

Continued

REAGENT or RESOURCE	SOURCE	IDENTIFIER
Polyclonal rabbit anti-SNX12 Antibody (PLA 1:100)	Invitrogen	Cat#PA5-99046; RRID: AB_2813659
Polyclonal rabbit anti-StrepII-tag Antibody (WB 1:2,000; PLA 1:450)	Abcam	Cat#ab76949; RRID: AB_1524455
Polyclonal rabbit anti-STX12 Antibody (PLA 1:100) (WB 1:500) (IP)	Proteintech	Cat#14259-1-AP; RRID: AB_2198222
Polyclonal rabbit anti-TAB1 Antibody (PLA 1:100)	Abcam	Cat#ab151408
Polyclonal rabbit anti-TMEM87B Antibody (PLA 1:100) (WB 1:500) (IP)	Invitrogen	Cat#PA5-57188; RRID: AB_2648735
Bacterial and virus strains		
E. coli XL-2 Blue Ultracompetent Cells	Agilent Technologies	Cat#200150
SARS-CoV-2 NL-02-2020 (NL)	European Virus Archive	BetaCoV/Netherlands/01/NL/2020; GISAID ID: EPI_ISL_413570; #010V-03903
SARS-CoV-2 Delta	Florian Schmidt and Bianca Schulte, University Hospital Bonn, Bonn, Germany	SARS-CoV-2 isolate of lineage B.1.617.2 N/A
SARS-CoV-2 Omicron BA.1	European Virus Archive	hCoV-19/Netherlands/NH-EMC-1720/ 2021 lineage B.1.1.529
SARS-CoV-2 Omicron BA.2 isolate harboring E T9 (PV58179)	Viviana Simon and Hala Alshammary, Mount Sinai Pathogen Surveillance Program, Mount Sinai Hospital, New York, USA	USA/NY-MSHSPSP- PV58179/2022; GISAID ID: EPI_ISL_12711111;
SARS-CoV-2 Omicron BA.2 isolate harboring E T9I (PV58079)	Viviana Simon and Hala Alshammary, Mount Sinai Pathogen Surveillance Program, Mount Sinai Hospital, New York, USA Sinai Hospital, New York, USA	USA/NY-MSHSPSP- PV58079/2022; GISAID ID: EPI_ISL_12711042
SARS-CoV-2 Omicron BA.5	Florian Schmidt and Bianca Schulte, University Hospital Bonn, Bonn, Germany	SARS-CoV-2 isolate of lineage B.1.1.529
SARS-CoV-2 Omicron XBB.1.5	Viviana Simon and Hala Alshammary, Mount Sinai Pathogen Surveillance Program, Mount Sinai Hospital, New York, USA	USA/NY-MSHSPSP- PV76648/2022; GISAID ID: EPI_ISL_17617932
rSARS-CoV-2 E T9	Arne Cordsmeier and Armin Ensser, Friedrich-Alexander University Erlangen-Nürnberg, Erlangen, Germany	Herrmann et al.[40]
rSARS-CoV-2 E T9I	This study.	N/A
VSV(GFP)ΔG*VSV-G	Karl-Klaus Conzelmann, University of Munich, Munich, Germany	N/A
VSV(GFP)ΔG*SARS-CoV-2: S	This study	N/A
VSV(GFP)ΔG*SARS-CoV-2: S, E T9	This study	N/A
VSV(GFP)ΔG*SARS-CoV-2: S, E T9I	This study	N/A
Chemicals, peptides, and recombinant proteins		
Acetonitrile (ACN)	VWR	Cat#20048.320
Agar	BD Biosciences	Cat#214010
Amphotericin B	Gibco	Cat#15290026
Bafilomycin A1	Santa Cruz Biotechnology	Cat#sc-201550
BamHI-HF	New England Biolabs	Cat#R3136L
BIT225 (*N*-Carbamimidoyl-5-(1-methyl-1*H*-pyrazol-4-yl)-2-naphthamide)	Klaus Klumpp, Gary Ewart and Michelle Miller of Biotron Limited	N/A
Blasticidin	InvivoGen	Cat#asnt-bl-1
Blocker Casein in PBS	Thermo Fisher Scientific	Cat#37528
Bovine serum albumin (BSA)	KPL	Cat#5140-0006

(*Continued on next page*)

Continued

REAGENT or RESOURCE	SOURCE	IDENTIFIER
Chameleon Duo Pre-stained Protein Ladder	LI-COR	Cat#928-60000
Chloroacetamide (CAA)	Sigma-Aldrich	Cat#75259
Complete protease inhibitor cocktail	Roche	Cat#05056489001
DABCO	Carl Roth	Cat#0718
4′,6-Diamidino-2-Phenylindole, Dihydrochloride (DAPI)	Invitrogen	Cat#D1306
DNase/RNase free water	Gibco	Cat#10977-035
Dulbecco's Modified Eagle Medium (DMEM)	Gibco	Cat#41965039
Dulbecco's Phosphate Buffered Saline (DPBS)	Gibco	Cat#14190-094
Duolink *In Situ* Detection Reagents FarRed	Sigma-Aldrich	Cat#DUO92013
Duolink *In Situ* PLA Probe Anti-Mouse MINUS	Sigma-Aldrich	Cat#DUO92004
Duolink *In Situ* PLA Probe Anti-Rabbit PLUS	Sigma-Aldrich	Cat#DUO92002
Dynabeads Protein G	Thermo Fisher Scientific	Cat#10004D
EcoRI-HF	New England Biolabs	Cat#R3101L
Ethylenediaminetetraacetic acid (EDTA)	Sigma-Aldrich	Cat#E9884
Formic acid (FA)	Sigma-Aldrich	Cat#47671-250ML-F
Fetal bovine serum (FBS)	Gibco	Cat#A5256701
Gentamicin	PAN-Biotech	Cat#15710-049
Gluta-MAX™	Thermo Fisher Scientific	Cat#35050061
HEPES	Thermo Fisher Scientific	Cat#15630080
HEPES	Carl Roth	Cat#6763.1
HEPES pH 7.4	Sigma-Aldrich	Cat#H3375
IFN-β	R&D Systems	Cat#8499-IF-010/CF
Immobilon-FL PVDF-Membrane	Merck	Cat#IPFL00010
L-glutamine	PAN-Biotech	Cat#P04-80100
Glycerol	Sigma-Aldrich	Cat#G5516
Glycerol	Sigma-Aldrich	Cat#49782
Guanidinium chloride	Sigma Aldrich	Cat#G3272
Lipofectamine3000	Invitrogen	Cat#L3000008
Lipofectamine RNAiMax Transfection Reagent	Invitrogen	Cat#13778150
Lys-C	WAKO Chemicals	Cat#125-05061
LysoTracker Deep Red	Invitrogen	Cat#2268303
Magnesium chloride ($MgCl_2$)	Sigma-Aldrich	Cat#M8266
Minimum Essential Medium Eagle (MEM)	Sigma-Aldrich	Cat#M4655
MEM Non-Essential Amino Acids	Gibco	Cat#11140050
β-mercaptoethanol	Sigma-Aldrich	Cat#444203
20x MES-SDS running buffer	Thermo Fisher Scientific	Cat#J62138.K2
Methanol (100%)	Merck	Cat#1060092511
Mowiol 4-88	Carl Roth	Cat#0713
Normocin	InvivoGen	Cat#ant-nr-1
NP-40	Sigma Aldrich	Cat#I3021
NuPAGE 4–12% Bis-Tris Gels	Invitrogen	Cat#NP0321BOX
Opti-MEM reduced serum media (Opti-MEM)	Gibco	Cat#31985047
Orange G	Sigma-Aldrich	Cat#O3756
Paraformaldehyde (PFA)	Santa Cruz Biotechnology	Cat#sc-281692
5x passive lysis buffer	Promega	Cat#E194A
Polyethyleneimine-hydrochlorid (PEI)	Sigma-Aldrich	Cat#764965-1G
Penicillin-Streptomycin	PAN-Biotech	Cat#P06-07100

(*Continued on next page*)

Continued

REAGENT or RESOURCE	SOURCE	IDENTIFIER
Protease inhibitor	Sigma-Aldrich	Cat#P2714
Proteinase K	Sigma-Aldrich	Cat#3115828001
Puromycin	InvivoGen	Cat#ant-pr-1
Rapamycin	Merck	Cat#553211-500UG
20-cm reverse-phase analytical column (75 μm diameter, 1.9 μm resin)	Dr. Maisch	Cat#ReproSil-Pur C18-AQ
Roswell Park Memorial Institute (RPMI) Medium 1640	Gibco	Cat#21875-034
Saponin	Sigma-Aldrich	Cat#47036
10x Semi dry blot transfer buffer	Thermo Fisher Scientific	Cat#J63664.K3
Sequencing grade modified trypsin	Promega	#V5111
Sodium chloride (NaCl)	Merck	Cat#106404
Sodium chloride (NaCl)	Sigma-Aldrich	Cat#S9888
Sodium dodecyl sulfate (SDS)	Sigma-Aldrich	Cat#8.22050
Sodium pyruvate	Thermo Fisher Scientific	Cat#11360039
Strep-II tagged beads	IBA Lifesciences GmbH	Cat#2-1201-025
Sucrose	Sigma-Aldrich	Cat#S9378-1KG
SuperSignal West Atto Ultimate Sensitivity Substrate	Thermo Fisher Scientific	Cat#A38556
TaqMan Fast Virus 1-Step Master Mix	Thermo Fisher Scientific	Cat#4444436
TransIT-LT1 Transfection Reagent	Mirus	Cat#MIR2306
TRIzol Reagent	Thermo Fisher Scientific	Cat#15596018
Tris(2-carboxyethyl)phosphine (TCEP)	Merck	Cat#75259
Tris-Cl	AppliChem GmbH	Cat#A2264
Tris-HCl	AppliChem GmbH	Cat#A2264
Tris-HCl	Sigma-Aldrich	Cat#T1503
Triton X-100	Sigma-Aldrich	Cat#T8787
0.05% Trypsin-0.02% EDTA	PAN Biotech	Cat#P10-023100
0.5% Trypsin-EDTA	Gibco	Cat#15400-054
Tryptone	Serva	Cat#48647.02
Torin-1	EZSolution	Cat#2353
Tween 20	Sigma-Aldrich	Cat#P9416
Whatman filter paper	VWR	Cat#588-3148
Yeast extract	Gibco	Cat#212750
Critical commercial assays		
CellTiter-Glo luminescent cell viability assay	Promega	Cat#G7571
COVID-19 Spike-ACE2 Binding Assay Kit	RayBioTech	Cat#CoV-ACE2S2-1
Direct-zol RNA Miniprep	Zymo Research	Cat#R2052
NEBuilder HiFi DNA Assembly Master Mix	New England Biolabs	Cat#E2621
Pierce Rapid Gold BCA Protein Assay Kit	Thermo Fisher Scientific	Cat#A53225
Q5 Site-Directed Mutagenesis	New England Biolabs	Cat#E0554S
QIAamp Viral RNA Mini Kit	Qiagen	Cat#52906
Quick-RNA Miniprep Kit	Zymo Research	Cat#R1055
SARS-CoV-2 (2019-nCoV) Spike Detection ELISA Kit	SinoBiological	Cat#KIT40591
SuperScript III Platinum One-Step qRT-PCR-Kit	Thermo Fisher Scientific	Cat#11732088
Deposited data		
Interactome data (Mass spectrometry)	PRIDE	PRIDE: PXD048080

(*Continued on next page*)

Continued

REAGENT or RESOURCE	SOURCE	IDENTIFIER
Source Data	Mendeley Repository	Mendeley Data: https://doi.org/10.17632/6gbt6bnbrh.1
Experimental models: Cell lines		
African green monkey: Vero E6	ATCC	CRL-1586; RRID: CVCL_0574
African green monkey: Vero E6-TMPRSS2-ACE2	Viviana Simon and Hala Alshammary, Mount Sinai Hospital, New York, USA	NR-54970; RRID: CVCL_C7NK
Human: A549	Andreas Pichlmair and Jyoti Vishwakarma Technical University of Munich, Munich, Germany)	N/A
Human: ATG5KO HEK293T	Konstantin Sparrer, Ulm University Medical Center, Ulm, Germany	N/A
Human: ATG5KO MRC5-ACE2	Ruth Serra-Moreno, University of Rochester, New York, USA	N/A
Human: Calu-3	Manfred Frick, Ulm University, Ulm, Germany	RRID: CVCL_0609
Human: Caco-2	Holger Barth, Ulm University Medical Center, Ulm, Germany	RRID: CVCL_0025
Human: HEK293T	ATCC	CRL-3216; RRID: CVCL_0063
Human: HEK293T/17	ATCC	CRL-11268
Human: HEK293T-GL (GFP-LC3B)	Konstantin Sparrer, Ulm University Medical Center, Ulm, Germany	Koepke, Winter et al.[34]
Human: HEK293T-T7RNAP-SARS-CoV-2 N	Arne Cordsmeier and Armin Ensser, Friedrich-Alexander University Erlangen-Nürnberg, Erlangen, Germany	Herrmann et al.[40]
Human: HeLa-GL (GFP-LC3B)	Konstantin Sparrer, Ulm University Medical Center, Ulm, Germany	Koepke, Winter et al.[34]
Human: MRC5-ACE2	Ruth Serra-Moreno, University of Rochester, New York, USA	N/A
Mouse: I1-Hybridoma cells	ATCC	CRL-2700; RRID: CVCL_G654
Oligonucleotides		
Human Abcg2-FAM-MGB primer probe	Thermo Fisher Scientific	Cat#Hs01053790_m1
Human GAPDH-VIC-TAMRA primer probe	Applied Biosystems	Cat#4310884E
Human Snx12-FAM-MGB primer probe	Thermo Fisher Scientific	Cat#Hs04999580_s1
Human Stx12-FAM-MGB primer probe	Thermo Fisher Scientific	Cat#Hs00295291_m1
Human Tab1-FAM-MGB primer probe	Thermo Fisher Scientific	Cat#Hs00196143_m1
Human Tmem87B-FAM-MGB primer probe	Thermo Fisher Scientific	Cat#Hs00262432_m1
For primers used for cloning see Table S1		
Human ABCG2 siRNA	Horizon Discovery ordered as SMARTPool	Cat#M-009924-01-0005
Human SNX12 siRNA	Horizon Discovery ordered as SMARTPool	Cat#M-013648-00-0005
Human STX12 siRNA	Horizon Discovery ordered as SMARTPool	Cat#M-018246-01-0005
Human TAB1 siRNA	Horizon Discovery ordered as SMARTPool	Cat#M-004770-02-0005
Human TMEM87B siRNA	Horizon Discovery ordered as SMARTPool	Cat#M-015008-00-0005
Recombinant DNA		
Bacmid: pBeloSARS-CoV-2	Arne Cordsmeier and Armin Ensser, Friedrich-Alexander University Erlangen-Nürnberg, Erlangen, Germany	Herrmann et al.[40]
Bacmid: pBeloSARS-CoV-2 E T9I	This study	N/A
Plasmid: pCG_SARS-CoV-2-Spike-Wuhan-1	Fabian Zech and Chiara Pastorio, Ulm University Medical Center, Ulm, Germany	Zech et al.[44]

(*Continued on next page*)

Continued

REAGENT or RESOURCE	SOURCE	IDENTIFIER
Plasmid: pLVX-EF1alpha-empty	This study	N/A
Plasmid: pLVX-EF1alpha-SARS-CoV-2-E–2xStrep-IRES-Puro	Nevan Krogan and David Gordon, University of California San Francisco, San Francisco, USA	Gordon, Jang, Bouhaddou, Xu, Obernier, White, O'Meara, Rezelj et al.[78]
Plasmid: pLVX-EF1alpha-SARS-CoV-2-E T9I-2xStrep-IRES-Puro	This study	N/A
Plasmid: pLVX-EF1alpha-SARS-CoV-2-E T11A-2xStrep-IRES-Puro	This study	N/A
Plasmid: pLVX-EF1alpha-SARS-CoV-2-E T9I T11A-2xStrep-IRES-Puro	This study	N/A
Plasmid: pLVX-EF1alpha-SARS-CoV-2-*M*-2xStrep-IRES-Puro	Nevan Krogan and David Gordon, University of California San Francisco, San Francisco, USA	Gordon, Jang, Bouhaddou, Xu, Obernier, White, O'Meara, Rezelj et al.[78]
Plasmid: pLVX-EF1alpha-SARS-CoV-2-ORF7a-2xStrep-IRES-Puro	Nevan Krogan and David Gordon, University of California San Francisco, San Francisco, USA	Gordon, Jang, Bouhaddou, Xu, Obernier, White, O'Meara, Rezelj et al.[78]
Plasmid: pLVX-EF1alpha-SARS-CoV-2-ORF7a V82A-2xStrep-IRES-Puro	This study	N/A
Plasmid: pLVX-EF1alpha-SARS-CoV-2-ORF7a T120I-2xStrep-IRES-Puro	This study	N/A
Plasmid: pLVX-EF1alpha-SARS-CoV-2-ORF8-2xStrep-IRES-Puro	Nevan Krogan and David Gordon, University of California San Francisco, San Francisco, USA	Gordon, Jang, Bouhaddou, Xu, Obernier, White, O'Meara, Rezelj et al.[78]
Plasmid: pTwist-empty	This study	
Plasmid: pTwist_EF1a_3xFLAG_opt TRIM3	Konstantin Sparrer, Ulm University Medical Center, Ulm, Germany	Hoenigsperger, Koepke et al.[79]
Plasmid: pTwist _SARS-CoV-2-ORF3a-2xStrep	Twist Bioscience	N/A
Plasmid: pTwist _SARS-CoV-2-ORF3a S26L-2xStrep	This Study	N/A
Plasmid: pTwist _SARS-CoV-2-ORF3a T223I-2xStrep	This Study	N/A
Software and algorithms		
Amsterdam Modeling Suite 2020	Software for Chemistry & Materials	http://www.scm.com
Corel Draw 2021	Corel Corporation	https://www.coreldraw.com/de/
FlowJo 10	BD Biosciences	http://www.flowjo.com
GraphPad Prism 10	GraphPad	https://www.graphpad.com
HOLE program	N/A	https://www.holeprogram.org/
Huygens Colocalization Analyzer	Scientific Volume Imaging	https://www.svi.nl
Huygens Professional 19.04 software	Scientific Volume Imaging	https://www.svi.nl
ImageJ (Fiji)	N/A	https://imagej.net/software/fiji
Image Studio Version 5.2	LI-COR	http://www.licor.com
Image Studio Lite Version 5.0.21	LI-COR	http://www.licor.com
LAS X imaging software	Leica Microsystems	https://www.leica-microsystems.com
MaxQuant 1.6.14	Max Planck Institute of Biochemisty	https://www.maxquant.org/
Perseus 0.01.	Max Planck Institute of Biochemisty	https://maxquant.net/perseus/
Simplicity 4.2	Berthold Technologies GmbH & Co. KG	https://www.berthold.com/en/
SoftMax Pro 7.0.3	Molecular Devices LLC	https://www.moleculardevices.com
Visual Molecular Dynamics (VMD 1.9.3)	Humphrey et al.[80]	https://www.ks.uiuc.edu/Research/vmd/
ZEN 2010	Zeiss	https://www.zeiss.com

EXPERIMENTAL MODEL AND STUDY PARTICIPANT DETAILS

Cell culture

All cells were cultured at 37°C at 5% CO_2 and 95% relative humidity. HEK293T, HEK293T/17, *ATG5* KO HEK293T,[79] and Vero E6 cells were cultivated in Dulbecco's Modified Eagle Medium (DMEM) containing 10% (v/v) heat-inactivated fetal bovine serum (FBS), 6.5 μg/mL gentamicin, and 2 mM L-glutamine. HEK293T cells are human embryonic kidney cells, which derived from a female fetus in 1973. Vero E6 cells derived from African green monkey kidney in 1979. Autophagy reporter HEK293T and HeLa cells stably expressing GFP-LC3B (GL) were reported previously.[34] HeLa cells originated from a human cervical cancer of a 31-year-old African American female in 1951. HEK293T-GL and HeLa-GL cells were cultivated in DMEM supplemented with 10% (v/v) heat-inactivated FBS, 6.5μg/ml gentamicin, and 2 mM L-glutamine. Caco-2 are human epithelial colorectal adenocarcinoma cells, derived from a 72-year-old white male in 1974. Caco-2 cells were maintained in DMEM supplemented with 20% (v/v) heat-inactivated FBS, 6.5 μg/mL gentamicin, and 2 mM L-glutamine. Calu-3 cells, derived from a human lung adenocarcinoma of a 25-year-old white male in 1975, were cultivated Minimum Essential Medium Eagle supplemented with 10% (v/v) heat-inactivated FBS (during viral infection) or 20% (v/v) FBS (during all other times), 100 mg/mL streptomycin, 100 U/ml penicillin and 2 mM L-glutamine. Vero E6 cells overexpressing ACE2 and TMPRSS2 were maintained in DMEM supplemented with 10% (v/v) heat-inactivated FBS, 1% (v/v) of 100x MEM Non-Essential Amino Acids (NEAA), 100 mg/mL streptomycin, 100 U/ml penicillin, 2 mM L-glutamine, 1 mM sodium pyruvate, 100 μg/mL of normocin and 3 μg/mL of puromycin. ACE2 overexpressing MRC5 cells were cultivated in DMEM supplemented with 20% (v/v) heat-inactivated FBS, 6.5 μg/mL gentamicin, and 2 mM L-glutamine. For *ATG5* KO MRC5-ACE2 cells 1 μg/mL Puromycin was additionally added to the medium. Mouse I1-Hybridoma cells were cultured in Roswell Park Memorial Institute (RPMI) Medium 1640 with 10% (v/v) heat-inactivated FBS, 100 mg/mL streptomycin, 100 U/ml penicillin, 2 mM L-glutamine. MRC-5 are human fetal lung fibroblast cells, derived from a 14-week-old male fetus in 1966. HEK293T cells expressing a T7 polymerase and SARS-CoV-2 N protein (HEK293T-T7RNAP-SARS-CoV-2 N)[40] for virus reconstitution were cultivated in DMEM supplemented with 10% (v/v) heat-inactivated FBS, 2 mM Gluta-MAX, 25 mM HEPES, 5 μg/mL blasticidin, 2 μg/mL puromycin. HEK293T and A549 cell lines for mass spectrometry experiments were cultured in DMEM supplemented with 10% (v/v) heat-inactivated FBS and 1% Penicillin-streptomycin. A549 are human lung carcinoma cells, derived from a 58-year-old white male in 1972. Purchased cell lines were authenticated by the respective vendor and were not validated further in our laboratory. All cell lines were tested to be mycoplasma free. The sex and gender of the cell lines had no impact on the design and results of this study.

Study participant details

The Mount Sinai Health System (MSHS) is one of the largest health care providers in the New York City metropolitan area. This health system supports a well-integrated pathogen surveillance infrastructure enabling real time monitoring of pathogens detected in people receiving care at one of the eight hospitals as well as at any of the many outpatient clinics. As part of the ongoing Surveillance Program over 10,000 SARS-CoV-2 genome sequences generated between March 2020 and December 2023 were searched. For this study viruses were isolated from swabs of two selected donors due to their viral sequence characteristics: USA/NY-MSHSPSP-PV58179/2022 isolated from a female patient with unknown age and USA/NY-MSHSPSP-PV58079/2022 isolated from a 40-year-old female patient. For the isolation of patient SARS-CoV-2 strains, approval for the Mount Sinai Pathogen Surveillance Program (MS-PSP) was obtained from the Mount Sinai Hospital (MSH) Institutional Review Board (IRB-13-00981).

METHOD DETAILS

Propagation of SARS-CoV-2

SARS-CoV-2 was propagated on different cell lines depending on the viral variant: Vero E6 (NL-02-2020, Delta), Calu-3 cells (Omicron BA.1, BA.5), or Vero E6 cells overexpressing ACE2 and TMPRSS2 (XBB.1.5 and BA.2 variants). To this end, 70–90% confluent cells in 75 cm^2 cell culture flasks were inoculated with the SARS-CoV-2 isolate (multiplicity of infection (MOI) of 0.03–0.1) in 3.5 mL serum-free medium MEM. The cells were incubated for 2 h at 37°C, before adding 20 mL medium containing 15 mM HEPES. The supernatants were harvested as soon as strong cytopathic effect (CPE) became apparent, cellular debris pelleted (5 min at 1,000 g), aliquoted, and stored at −80°C until further use.

SARS-CoV-2 isolates

Residual nasopharyngeal swab specimens from patients with COVID-19 were banked by the Mount Sinai Pathogen Surveillance Program after the completion of the diagnostic process as reported previously.[38,39] Replication-competent SARS-CoV-2 Omicron BA.2 isolates harboring E T9 (PV58179) or E T9I (PV58079) were cultured by inoculating VeroE6-TMPRSS2-ACE2 cells with 200 μL of viral transport media from the nasopharyngeal swab specimen. The culture media were supplemented with 2% heat-inactivated FBS, 100 μg/mL normocin, and 0.5 μg/mL amphotericin B, and maintained for a maximum of 10 days. Upon the appearance of cytopathic effects, culture supernatants were collected, clarified by centrifugation (3,739g for 5 min) and the sequence verified.

Generation and propagation of a rSARS-CoV-2

Recombinant SARS-CoV-2 were generated based on the bacmid pBeloSARS-CoV-2.[40] In brief, the sequence encoding for E was replaced via homologous recombination by a kanamycin resistance cassette with *AscI* restriction enzyme sites at each end and using the primers dE-Asc-KanS-FP and dE-Asc-KanS-RP. Subsequently, the kanamycin resistance cassette was removed by digestion and a respective PCR fragment containing the E T9I mutation and with overlapping ends was introduced by Gibson assembly using the NEBuilder HiFi DNA Assembly Master Mix. This PCR fragment was amplified using cDNA from a patient sample containing the E T9I mutation with the primers Efwd and Erev. The resulting bacmid was transformed in *E. coli* and recovered by DNA isolation. The correct assembly was verified by Next Generation Sequencing of the full bacmid. The recovery of infectious virus was performed by transfection of HEK293T-T7RNAP-SARS-CoV-2 N cells and passaging on Caco-2 cells. The method has been described previously.[40,81]

Analyzing growth of rSARS-CoV-2

Calu-3, MRC5-ACE2 and *ATG5* KO MRC5-ACE2 cells were seeded 24 h prior to infection (3×10^4 per well of a 96-well plate). The cells were treated with 250 nM Torin-1 2 h before infection with rSARS-CoV-2 E T9 or rSARS-CoV-2 E T9I (MOI 0.05). After 6 h post infection, the medium was replaced by fresh medium or medium containing 250 nM fresh Torin-1. Viral supernatants were collected at 6 h, 24 h and 48 h post infection and cells were harvested 72 h post infection. The samples were heat inactivated and digested with proteinase K. Samples collected from MRC5-ACE2 and *ATG5* KO MRC5-ACE2 cells were additionally treated 1:1 with TRIzol for transportation.

Impact of autophagy on SARS-CoV-2 WT

1.5×10^5 Calu-3 cells/well were seeded in 24-well plates. 24 h post-seeding cells were either left untreated or were stimulated with increasing amounts of Torin-1 (0.016, 0.063, 0.25 or 1 μM). Two hours post-treatment, Calu-3 cells were infected with various SARS-CoV-2 strains (MOI 0.05). Six hours post-infection, the cells were washed once with Dulbecco's Phosphate Buffered Saline (DPBS) and supplemented with fresh medium or medium containing increasing amounts of Torin-1 (0.016, 0.063, 0.25, 1 μM). Supernatants were harvested at 6 h (for wash control) and 48 h post-infection for qRT-PCR and Tissue culture infectious dose 50 (TCID50) analyses.

TCID50 determination

1.5×10^4 Vero E6 cells/well were seeded in 96-well F-bottom plates in 100 μL medium and incubated overnight. SARS-CoV-2 stocks or infectious supernatants were serially diluted and 100 μL of the dilution were added to the cells (final dilutions $1{:}10^1$ to $1{:}10^{10}$). The cells were monitored for cytopathic effects over the course of 5 days. TCID50/mL was calculated according to the Reed-Muench method.[82]

siRNA-mediated knockdown

1×10^5 HEK293T-GL cells/well were grown in 500 μL medium in 24-well plates and one day later transfected with siRNA using Lipofectamine RNAiMax Transfection Reagent and Opti-MEM reduced serum media according to the manufacturer's instructions. Two days post transfection with siRNA, cells were either harvested for qRT-PCR analysis or transfected with plasmids encoding for E or E T9I harboring a StrepII tag (1 μg DNA/well) by using 2 μL 1x PEI and 100 μL Opti-MEM reduced serum media per well. In brief, 50 μL Opti-MEM were mixed with 2 μL 1x PEI and incubated for 5 min. Secondly, 50 μL Opti-MEM were mixed with 1 μg DNA. Afterward both mixes were combined and after incubation (20 min, RT), the transfection mix was added to the cells. One day later the cells were further processed for immunoblotting and autophagosome measurement by flow cytometry (FACS-Canto II).

qRT-PCR

Total RNA of the supernatants collected from SARS-CoV-2 infected Calu-3 cells 48 h post-infection were isolated using the QIAamp Viral RNA Mini Kit according to the manufacturer's instructions. To isolate viral RNA from rSARS-CoV-2 infected MRC5-ACE2 WT or *ATG5* KO cells the Direct-zol RNA Miniprep kit was used following the manufacturer's instructions. To determine the SARS-CoV-2 N levels quantitative real-time PCR (qRT-PCR) was performed as previously described[19] using TaqMan Fast Virus 1-Step Master Mix and an StepOnePlus Real-Time PCR System (96-well format, fast mode). For qRT-PCR the SARS-CoV-2 N primer probe HKU-NP and the primers SARS-CoV-2 N_F (HKU-NF) and SARS-CoV-2 N_R (HKU-NR) were used (see Table S1). Synthetic SARS-CoV-2 RNA was used as a quantitative standard to determine viral copy numbers. All PCR reactions were run in technical duplicates. RNA of siRNA transfected cells was isolated using the Quick-RNA Miniprep Kit according to the manufacturer's instructions. To determine the KD efficiency, reverse transcription and qRT-PCR was performed in one step using the SuperScript III Platinum Kit on a StepOnePlus Real-Time PCR System according to the manufacturer's instructions. TaqMan probes for each individual KD gene and for GAPDH were acquired as premixed TaqMan Gene Expression Assays and added to the reaction. Expression level for each target gene was calculated by normalizing against GAPDH using the ΔΔCT method.

Impact of autophagy induction on IFITMs

0.7×10^6 Calu-3 cells/well were seeded in 6-well plates. 24 h post-seeding cells were left untreated or were stimulated with increasing amounts of Torin-1 (0.016, 0.063, 0.25 or 1 μM). As positive control for upregulation of IFITM expression, cells were treated with 1000 U IFN-β. 24 h post-treatment whole-cell lysates for SDS-PAGE and immunoblotting were prepared.

Cloning and origin of expression constructs

Plasmids encoding SARS-CoV-2 E-StrepII (pLVX-EF1alpha-SARS-CoV-2-E−2xStrep-IRES-Puro), SARS-CoV-2 M-StrepII (pLVX-EF1alpha-SARS-CoV-2-*M*-2xStrep-IRES-Puro), SARS-CoV-2 ORF7a-StrepII (pLVX-EF1alpha-SARS-CoV-2-ORF7a-2xStrep-IRES-Puro) and ORF8-StrepII (pLVX-EF1alpha-SARS-CoV-2-ORF8-2xStrep-IRES-Puro) were a kind gift from Nevan Krogan.[78] A plasmid encoding SARS-CoV-2 E 9I-StrepII was generated using pLVX-EF1alpha-SARS-CoV-2-E−2xStrep-IRES-Puro. To this end, the template vector was linearized with the restriction enzymes EcoRI-HF and BamHI-HF. All site directed mutagenesis was performed using the NEBuilder HiFi DNA Assembly Master Mix according to the manufacturer's instructions. To introduce the T9I mutation in E the primers E-T9I_F and E-T9I_R were used. SARS-CoV-2 E T11A-StrepII was generated using the template pLVX-EF1alpha-SARS-CoV-2-E−2xStrep-IRES-Puro and the primers E-T11A_F and E-T11A_R. SARS-CoV-2 E T9I T11A-StrepII was generated using pLVX-EF1alpha-SARS-CoV-2-E T9I-2xStrep-IRES-Puro as template and the primers E-T9I + T11A_F and E-T9I + T11A_R. ORF7a 120I-StrepII or ORF7a 82A-StrepII were generated by using pLVX-EF1alpha-SARS-CoV-2-ORF7a-2xStrep-IRES-Puro as a template and primers ORF7a-T120I_F and ORF7a-T120I_R or primers ORF7a-V82A_F and ORF7a-V82A_R. pLVX-EF1alpha was constructed using Q5 Site-Directed Mutagenesis according to the manufacturer's instructions with pLVX-EF1alpha-SARS-CoV-2-ORF8-2xStrep-IRES-Puro as template and pLVX-EF1alpha-empty-F and pLVX-EF1alpha-empty-R as primers. ORF3a 26L-StrepII and 223I-StrepII were cloned by Q5 Site-Directed Mutagenesis with pTwist_SARS-CoV-2-ORF3a-2xStrep as template and the primers ORF3a-S26L_F and ORF3a-S26L_R or primers ORF3a-T223I_F and ORF3a-T223I_R. pTwist-empty Vector was constructed using Q5 Site-Directed Mutagenesis, pTwist_EF1a_3xFLAG_opt TRIM3[79] as template and the primers pTwist-empty-F and pTwist-empty-R. All primers are listed with their sequence in Table S1. pCG_SARS-CoV-2-Spike-Wuhan-1 was previously described.[44] pTwist_SARS-CoV-2-ORF3a-2xStrep was purchased from Twist Bioscience.

Generation of VSV-pseudoparticles

To produce pseudotyped VSVΔG-GFP particles, HEK293T WT and *ATG5* KO cells were transfected with Spike (HU-1), E (Hu-1) or E T9I expression constructs (in total 3 μg DNA/well) in 6-well format by using per well 10 μL 1x polyethyleneimine-hydrochlorid (PEI) (1 mg/mL in H_2O) and 500 μL Opti-MEM reduced serum media. In brief, 250 μL Opti-MEM was mixed with 10 μL 1x PEI and incubated for 5 min. Next, 250 μL Opti-MEM was mixed with 3 μg DNA. Both solutions were combined and incubated for 20 min at RT, then added on cells. 24h post-transfection the cells were infected with VSV(GFP)ΔG*VSV-G (MOI 3). 24 h post infection, cells and supernatants containing VSV(GFP)ΔG*S*E particles were harvested. Cell debris were removed by centrifugation for 4 min at 500 x g.

VSV-pseudoparticle assays

6×10^3 Caco-2 cells or MRC5-ACE2 (WT and *ATG5* KO) cells were seeded in 384-well plates in 25 μL medium. On the next day, the cells were treated with 10 μL Torin-1 (final concentration on cells 0.5 μM) or medium for 4 h and afterward infected with 35 μL of supernatant containing VSVΔG-GFP*S*Epp. Residual particles carrying VSV-G were blocked by adding 10% (v/v) of I1 hybridoma supernatant. GFP-positive cells were automatically counted 22 h post-infection by using Cytation 3 microplate reader.

Spike ELISA

Supernatants containing VSVΔG-GFP*S*Epp were analyzed for their S content by using a SARS-CoV-2 (2019-nCoV) Spike Detection ELISA Kit. Samples were diluted 1:200 in 1x dilution buffer provided by the Kit. The ELISA was performed according to the manufacturer's recommendations. Absorbance at 450 nm was detected using the Vmax kinetic microplate reader and the software SoftMax Pro 7.0.3.

Spike-ACE2 interaction assay

Supernatants containing VSVΔG-GFP*S*Epp were added on a cushion of 20% sucrose in PBS and centrifuged for 90 min at 4°C and 20,817 x g. The pellet was lysed in 12 μL transmembrane lysis buffer (50mM HEPES pH 7.4, 150 mM NaCl, 1% Triton X-100, 5 mM ethylenediaminetetraacetic acid (EDTA)) supplemented with 1:500 protease inhibitor and heated up for 10 min at 95°C. The interaction between Spike and ACE2 was analyzed using a COVID-19 Spike-ACE2 Binding Assay Kit. In brief, 10 μL of the lysates were mixed with 40 μL of 1x assay diluent buffer and added to the ACE2 coated wells. After 2 h incubation shaking at RT, the wells were washed 3 times with 200 μL 1x wash buffer and subsequently incubated with 100 μL monoclonal mouse anti-V5 antibody for 1 h at RT. After washing, 100 μL HRP-conjugated anti-IgG mouse was added for 1h while shaking. Next, the wells were washed and 50 μL TMB one-step substrate reagent (provided by the kit) added for 30 min while shaking in the dark. The reaction was stopped by adding 50 μL stop solution and the absorbance was detected at 450 nm with a baseline correction of 650 nm using the Vmax kinetic microplate reader and the software SoftMax Pro 7.0.3.

Autophagosome measurement by flow cytometry

4.5×10^4 HEK293T cells stably expressing GFP-LC3B (GL) cells were transiently reverse transfected with 200 ng expression vector in 96-well F-bottom plates by using 2 μL 1x PEI/μg DNA and 17 μL Opti-MEM reduced serum media.[34] The next day, the medium was replaced with 100 μL fresh medium. Cells were optionally stimulated with 0.2–5 μM BIT225 for 24 h or 0.25 μM Bafilomycin A1 for 4 h. 48 h post-transfection, the supernatant was removed and the cells were detached using Trypsin/EDTA 0.05%/0.02%. The harvested cells were washed with DPBS and treated with DPBS containing 0.05% Saponin for 20 min at 4°C for permeabilization. Subsequently, the cells were washed twice with DPBS to wash out the non-membrane bound GFP-LC3B and fixed in 2% paraformaldehyde (PFA). The mean fluorescence intensity (MFI) of membrane-bound GFP-LC3B was then detected by flow cytometry on a FACSCanto II. The MFI value of the control was used as baseline and subtracted.

Immunofluorescence microscopy

1×10^5 HeLa-GL cells/well were grown on coverslips with 500 μL medium in 24-well plates and one day later transfected with a control vector or expression vectors for SARS-CoV-2 E (Hu-1) or E T9I by using Opti-MEM reduced serum media and TransIT-LT1 Transfection Reagent according to the manufacturer's instructions. The supernatant was removed 6 h post-transfection and 500 μL fresh medium was added to the cells. As a positive control, cells were treated with 1 μM Rapamycin 24 h before harvesting. 48 h post-transfection the cells were washed twice with DPBS, fixed with 4% PFA for 20 min at RT. Blocking and permeabilization was performed by using DPBS with 0.5% Triton X-100 and 5% FBS for 1 h at RT. After washing with DPBS, the cells were stained with the following primary antibodies diluted in DPBS with 1% FBS for 2 h at 4°C: Monoclonal mouse anti-StrepII-tag, monoclonal rabbit anti-LAMP1 and monoclonal rabbit anti-Rab7 antibody. Subsequently, the cells were washed three times with DPBS supplemented with 0.1% Tween 20. Fluorescently labeled secondary antibodies Goat anti-Mouse IgG (H + L) Highly Cross-Adsorbed AF568, Goat anti-Rabbit IgG (H + L) Highly Cross-Adsorbed AF647 as well as DAPI (4′,6-Diamidino-2-Phenylindole, Dihydrochloride) were diluted in DPBS with 1% FBS and incubated on the slips for 2 h at 4°C. Afterward, the cells were washed three times with DPBS/0.1% Tween 20 and additionally once with deionized water. The coverslips were mounted on microscope slides by using mowiol mounting medium (10% (w/v) Mowiol 4–88, 25% (w/v) Glycerol, 50% (v/v) Tris-Cl at 0.2 M pre-adjusted to pH 8.5 and 2.5% (w/v) DABCO) and then dried overnight at 4°C. Images were captured using a Zeiss LSM 710 confocal laser scanning microscope using the ZEN imaging software or Leica DMi8 confocal microscope using the LAS X imaging software. Co-localization analysis was performed using the Huygens Professional 19.04 software, and the Pearson coefficients were calculated via the "Huygens Colocalization Analyzer". Superresolution images were acquired using a Zeiss LSM 980 microscope and an Airyscan 2 detector. Autophagosome counts (GFP-LC3B puncta) per cell were determined using Fiji ImageJ. In brief, the channels were separated and the GFP-channel was used for quantification as previously described.[34] Then, background removal and smoothing were performed, a threshold was applied and the total area of the particles was determined.

Cell viability analysis

The supernatant of treated cells was removed and cells were then lysed in 1x passive lysis buffer (5x passive lysis buffer diluted in deionized water). Next, the CellTiter-Glo luminescent cell viability assay according to the manufacturer's instructions was performed and the luminescent was measured by using an Orion II microplate Luminometer (Berthold, Bad Wildbad, Germany) and the software Simplicity 4.2.

Whole-cell and supernatant lysates

For preparing whole-cell lysates (WCL) cells were washed with DPBS, centrifuged for 4 min at 300 x g and lysed in transmembrane lysis buffer supplemented with 1:500 protease inhibitor for 10 min on ice. Cell debris were pelleted by centrifugation for 20 min at 4°C and 20,000 x g and the total protein concentration of the cleared lysate was determined using the Pierce Rapid Gold BCA Protein Assay Kit according to the manufacturer's protocol. The samples were adjusted to the same protein concentration with transmembrane lysis buffer containing 1:500 protease inhibitor. For preparing cell-free lysates (CFL) of supernatant, cell debris were removed by centrifugation for 4 min at 500 x g and the supernatants were transferred to fresh reaction tubes. After layering the supernatant on a cushion of 20% sucrose in PBS, samples were centrifuged for 90 min at 4°C and 20,817 x g and the pellet was resuspended in transmembrane lysis buffer containing 1:500 protease inhibitor.

SDS-PAGE and immunoblotting

SDS-PAGE and immunoblotting was performed as previously described.[34] In brief, whole-cell and supernatant lysates were mixed with 6x protein sample loading buffer (187.5 mM Tris-HCl adjusted to pH 6.8, 75% (v/v) glycerol, 6% (w/v) SDS, 0.3% (w/v) Orange G, 15% (v/v) β-mercaptoethanol dissolved in deionized water) to a final concentration of 1x and heated up to 95°C for 10 min before use. For protein separating, the samples were loaded on NuPAGE 4–12% Bis-Tris Gels and the gels were running in 1x MES-SDS running buffer (20x MES-SDS running buffer diluted in deionized water) for 90 min at 90 V. Next, the separated proteins were semi-dry blotted onto an Immobilon-FL PVDF-Membrane at a constant voltage of 30 V for 30 min. After blocking in Blocker Casein in PBS for 1 h, the proteins on the membrane were stained with primary antibodies diluted in PBS-T (1x PBS with 0.2% (v/v) Tween 20 and 0.1% (v/v) Blocker Casein in PBS) for 2 h at RT or overnight at 4°C. After incubation with the primary antibodies, the membrane was washed three times with PBS-T for 5 min at RT. Subsequently, the membrane was incubated in IRDye secondary antibodies diluted in

PBS-T. The following IRDye secondary antibodies were used in this study: IRDye 680RD Goat anti-Rabbit IgG, IRDye 800CW Goat anti-Mouse IgG, IRDye 680RD Goat anti-Rat IgG, IRDye 800CW Goat anti-Rat IgG and Goat anti-rabbit IgG H&L (HRP). After three times washing with PBS-T, the fluorescent signal of the IRDye secondary antibodies or the HRP after incubating the membrane with SuperSignal West Atto Ultimate Sensitivity Substrate for 1 min was detected using an LI-COR Odyssey (LI-COR, Lincoln, NE, US) and the Image Studio Version 5.2 software. Image processing and quantification of band intensities were analyzed by using the software Image Studio Lite Version 5.0.21.

Co-immunoprecipitation

Five million HEK293T cells were seeded in 10cm dishes with 10 mL medium and one day later transiently transfected with 12 μg DNA/dish with a control vector or the SARS-CoV-2 E T9I expression vector by using 2 μL 1x PEI/μg DNA and 1 mL/dish Opti-MEM reduced serum media. In brief, 500 μL Opti-MEM were mixed with 24 μL 1x PEI and incubated for 5 min. Subsequently, 500 μL Opti-MEM were mixed with 12 μg DNA and added to the Mix of Opti-MEM and PEI. After 20 min of incubation at RT, the mix was added to the cells. 48 h post transfection, the cells were harvested and WCLs were prepared. A part of the WCLs were saved as input sample for immunoblotting. The remaining E T9I WCL was equally distributed to magnetic beads (Dynabeads Protein G) which were before twice washed with PBS-T, incubated with 1 μg/10 μL beads primary antibody (polyclonal rabbit anti-TMEM87B, polyclonal rabbit anti-ABCG2, polyclonal rabbit anti-STX12, Normal Rabbit IgG Polyclonal Antibody control) for 30 min at RT on a rotating shaker and twice washed with transmembrane lysis buffer containing 1:500 protease inhibitor. The WCL were incubated on the beads for 4h at 4°C on a rotating shaker. Subsequently, beads were collected using a magnetic rack and washed five times with cold transmembrane lysis buffer containing 1:500 protease inhibitor. Finally, the beads were taken up in 50 μL in 1x protein sample loading buffer and the supernatant prepared for immunoblotting.

Proximity ligation assay (PLA)

6×10^4 HeLa cells were seeded on glass cover slips in 24-well plates one day prior transient transfection using Lipofectamine3000 with plasmids encoding E or E T9I harboring a StrepII tag according to the manufacturer's instructions. Cells were fixed 30 h post transfection in 3.7% PFA. Cell membranes were permeabilized with 0.5% Triton and blocked with 5% BSA. PLA staining was performed as previously described.[83,84] Primary antibodies used: Polyclonal rabbit anti-SNX12 antibody, polyclonal rabbit anti-STX12 antibody, polyclonal rabbit anti- TAB1 antibody, polyclonal rabbit anti-TMEM87B antibody, monoclonal mouse anti-ABCG2 antibody, polyclonal rabbit anti-StrepII-tag antibody, monoclonal mouse anti-StrepII-tag antibody. PLA probes and reagents used: Duolink *In Situ* PLA Probe Anti-Rabbit PLUS, Duolink *In Situ* PLA Probe Anti-Mouse MINUS, Duolink *In Situ* Detection Reagents FarRed. Imaging was conducted using a Zeiss LSM710 confocal microscope. Quantification of PLA foci was carried out with the ImageJ (Fiji) software.

Molecular modeling of SARS-CoV-2 E

The initial atomic positions were derived from the SARS-CoV-2 Envelope Protein Transmembrane domain as reported in the 7k3g entry of the Protein DataBank. Equilibration at 300 K for 0.5 ns was performed by ReaxFF[85] (reactive molecular dynamics) simulations using the Amsterdam Modeling Suite 2020. After equilibration, the amino acids of the Envelope Protein were replaced by the corresponding amino acids, together with the necessary modifications. Subsequently, an additional equilibration step (300 K for 0.5 ns) was performed by ReaxFF simulations in the NVT ensemble over 25 ps, with the system coupled to a Berendsen heat bath (held at T = 300 K with a coupling constant of 100 fs). Distances were calculated by averaging over these simulations. The program Visual Molecular Dynamics (VMD 1.9.3) was used for all visualizations.[80] The HOLE program was used to visualize the ion channel.[86]

Phylogenetic and mutation abundance analyses

The phylogenetic trees were derived from Nextstrain at indicated timepoints.[87,88] Abundance of the mutations in sequenced strains in the population was derived from data on Covspectrum.[36]

Interactome studies of E-expressing cells

HEK293T/17 cells were used to generate lentivirus for the Strep-II tagged E proteins. A549 cells (15×10^6 cells per 15 cm dish) were transduced with lentiviral vectors encoding E proteins with 2.5 μg/mL puromycin selection. Cell pellets from two 15-cm dishes were used and lysed in lysis buffer (50 mMs Tris-HCl pH 7.5, 100 mM NaCl, 1.5 mM $MgCl_2$, 0.2% (v/v) NP-40, 5% (v/v) glycerol, complete protease inhibitor cocktail, 0.5% (v/v) 750 U/μl Sm DNase). Further they were sonicated (15 min, 30 s on, 30 s off, high settings; Bioruptor, Diagenode). The protein lysates were normalized to 1 mg/mL for their concentration and subjected to affinity precipitation using 15 μL Strep-II tagged beads with a constant agitation at 4°C overnight. Subsequent washes with lysis buffer and washing buffer (50 mM Tris-HCl pH 7.5, 100 mM NaCl, 1.5 mM $MgCl_2$, 5% (v/v) glycerol) were performed to remove non-specifically bound proteins. The enriched proteins were denatured, reduced, alkylated and digested by addition of 180 μL digestion buffer (0.6 M guanidinium chloride), 1 mM tris(2-carboxyethyl)phosphine (TCEP), 4 mM chloroacetamide (CAA), 100 mM Tris-HCl pH 8, 0.5 μg Lys-C and 0.5 μg sequencing grade modified trypsin at 30°C overnight at 300 rpm shaking. Three layers of C18 Empore filter discs (3M) were used to prepare the stage tips and peptide purification was performed. The purified peptides were subjected to LC-MS/MS. Peptides were loaded on a 20-cm reverse-phase analytical column (75 μm diameter) and separated using an EASY-nLC 1200 system

(Thermo Fisher Scientific, Waltham, MA, US). A binary buffer system consisting of buffer A (0.1% formic acid (FA) in H_2O) and buffer B (80% acetonitrile (ACN), 0.1% FA in H_2O) with a 90-min gradient (5–30% buffer B (65 min), 30–95% buffer B (10 min), wash out at 95% buffer B (5 min), decreased to 5% buffer B (5 min), and 5% buffer B (5 min)) was used at a flow rate of 300 mL per min. Eluting peptides were directly analyzed on a Q-Exactive HF mass spectrometer in data-dependent acquisition (DDA) mode (Thermo Fisher Scientific, Waltham, MA, US). Data-dependent acquisition included repeating cycles of one MS1 full scan (300–1 650 m/z, R = 60 000 at 200 m/z) at an ion target of 3×10^6 with injection time of 20 ms. For MS2 scans the top 15 intense isolated and fragmented peptide precursors (R = 15 000 at 200 m/z, ion target value of 1×10^5, and maximum injection time of 25 ms) were recorded. Dynamic exclusion, isolation window of the quadrupole, and HCD normalized collision energy were set to 20 s, 1.4 m/z, and 27%, respectively.

Data processing and analysis of MS

Raw MS data files of AP–MS experiments conducted in DDA mode were processed with MaxQuant (version 1.6.14) using the standard settings and label-free quantification (LFQ) enabled (LFQ min ratio count 1, normalization type none, stabilize large LFQ ratios disabled). Spectra were searched against forward and reverse sequences of the reviewed human proteome including isoforms (UniprotKB, release 2019.10) and Strep-II tagged E proteins of SARS-CoV-2 strains and Strep-II tagged GFP protein by the built-in Andromeda search engine.[89] Peptide and protein identification was controlled by a False Discovery Rate (FDR) of 0.01. Perseus was used to analyze the output of MaxQuant.[90] Protein groups identified as known contaminants or reverse sequence matches were excluded from the analysis. Only proteins with a minimum of two LFQ quantifications in at least one group of replicate experiments ($n = 4$) for a specific bait were considered for the analysis. Missing values were imputed using normal distribution, whose standard deviation was defined as 30% and the mean was offset by -1.8 s.d. of the data distribution of the real intensities observed in the corresponding mass spectrometry run, respectively.

QUANTIFICATION AND STATISTICAL ANALYSIS

Statistical analysis

Statistical analyses were performed using GraphPad Prism 10. P-values were determined using a two-tailed Student's t test with Welch's correction. Unless otherwise stated, data are shown as the mean of at least three biological replicates ±SEM. Significant differences are indicated as: *, $p < 0.05$; **, $p < 0.01$; ***, $p < 0.001$. Unless otherwise specified, not significant (ns) differences are not indicated. Statistical parameters are further specified in the figure legends.